Published in final edited form as:

Ann Biomed Eng. 2010 April ; 38(4): 1288–1313. doi:10.1007/s10439-010-9949-x.

Quantification of Hemodynamics in Abdominal Aortic Aneurysms During Rest and Exercise Using Magnetic Resonance Imaging and Computational Fluid Dynamics

Andrea S. Les[1], **Shawn C. Shadden**[2], **C. Alberto Figueroa**[1], **Jinha M. Park**[3], **Maureen M. Tedesco**[4], **Robert J. Herfkens**[5], **Ronald L. Dalman**[4], and **Charles A. Taylor**[1,†]

[1] Department of Bioengineering, Stanford University, Stanford CA

[2] Department of Mechanical and Aerospace Engineering, Illinois Institute of Technology, Chicago, IL

[3] Department of Radiology, University of California, San Diego CA

[4] Division of Vascular Surgery, Stanford University, Stanford CA

[5] Department of Radiology, Stanford University, Stanford CA

Abstract

Abdominal aortic aneurysms (AAAs) affect 5-7% of older Americans. We hypothesize that exercise may slow AAA growth by decreasing inflammatory burden, peripheral resistance, and adverse hemodynamic conditions such as low, oscillatory shear stress. In this work, we use magnetic resonance imaging and computational fluid dynamics to describe hemodynamics in eight AAAs during rest and exercise using patient-specific geometric models, flow waveforms, and pressures as well as appropriately resolved finite-element meshes. We report mean wall shear stress (MWSS) and oscillatory shear index (OSI) at four aortic locations (supraceliac, infrarenal, mid-aneurysm, and suprabifurcation) and turbulent kinetic energy over the entire computational domain on meshes containing more than an order of magnitude more elements than previously reported results (mean: 9.0-million elements; SD: 2.3M; range: 5.7-12.0M). MWSS was lowest in the aneurysm during rest 2.5 dynes/cm^2 (SD: 2.1; range: 0.9-6.5) and MWSS increased and OSI decreased at all four locations during exercise. Mild turbulence existed at rest, while moderate aneurysmal turbulence was present during exercise. During both rest and exercise, aortic turbulence was virtually zero superior to the AAA for seven out of eight patients. We postulate that the increased MWSS, decreased OSI, and moderate turbulence present during exercise may attenuate AAA growth.

Keywords

Turbulence; Mean Wall Shear Stress; Oscillatory Shear Index; Mesh Independence; Flow Waveforms; Blood Pressure; Windkessel Boundary Condition; Patient-Specific

[†]Corresponding Author: Charles A. Taylor, Ph.D., James H. Clark Center, Room E350B, 318 Campus Drive, Stanford, CA 94305-5431, Phone: (650) 725-6128, Fax: (650) 725-9082, taylorca@stanford.edu.

Introduction

Abdominal aortic aneurysms (AAAs), defined as a 1.5-fold or more enlargement of the abdominal aorta, affect 5-7% of Americans over age 60 and kill approximately 9,000 people each year.[17,18,49] Risk factors for AAA include male gender, advanced age, cigarette smoking, heritable predisposition, and atherosclerotic disease.[31] Because no effective medical therapy exists for AAA patients, and because on average AAAs enlarge at a predictable rate,[8] most AAA patients postpone treatment until their aneurysm diameter reaches the threshold for surgical repair: 4.5 cm for women and 5.5 cm for men.[9] This threshold represents the point at which the risk of rupture is thought to outweigh the risk of surgical intervention.

Inflammation, increased peripheral resistance, and adverse/pro-inflammatory localized hemodynamic conditions, including low and oscillatory wall shear stress, are all thought to play a critical role in AAA formation. On the micro-scale, inflammatory processes such as recruitment of leukocytes into the aortic wall mediated by elastin degradation products[19] and chemokines,[29] phagocyte infiltration resulting in pro-inflammatory cytokines[40] and reactive oxygen species,[33] and the production of matrix metalloproteinases such as MMP-9 by macrophages[59] are all thought to instigate or promote AAA formation and growth.[12] On the macro-scale, patients with increased peripheral resistance caused by chronic spinal cord injury,[67] severe peripheral vascular disease,[1] and above the knee amputation[63] have been shown to have a 2.9, 4.2, and 5.3-fold increased rate of AAA, respectively, compared to control populations. Lastly, adverse/pro-inflammatory hemodynamic conditions such as low and oscillatory wall shear stress, as well as the presence of recirculation zones are also hypothesized to augment AAA development. In the human abdominal aorta, a correlation between low and/or oscillatory wall shear stress and atherosclerosis, which shares many of the same disease mechanisms as AAAs, has been demonstrated by autopsy,[11] as well as by experimental[36] and computational methods.[53] Furthermore, a correlation between regions of low wall shear stress and growth of intracranial aneurysms has recently been elucidated.[7] In addition, it has been demonstrated that regions of slow and/or recirculating flow correlate with regions of thrombus deposition in basilar aneurysms,[45] and a similar relationship has been proposed for abdominal aortic aneurysms.[5,48] A more complete review of biomechanical factors in aneurysm formation can be found in a recent paper by Humphrey and Taylor.[25]

We have proposed a new medical therapy for AAAs whereby lower limb exercise may slow or halt the growth of AAAs by decreasing inflammatory burden, peripheral resistance, and adverse hemodynamic conditions in the abdominal aorta.[13] Aside from reducing all-cause mortality,[38] exercise has been shown to effect potentially salutary increases in shear stress in the abdominal aortas of both young[53,54] and old people.[10] Furthermore, Nakahasi et al. and Hoshina et al. showed that increasing infrarenal flow through experimentally-created AAAs via a downstream arterio-venous fistula increased antioxidative enzyme expression, restricted reactive oxygen species production,[39] and limited AAA enlargement in rats.[23,39] Despite these promising studies, it is not known whether exercise may slow AAA growth in humans. This question is the basis of a National Institutes of Health (NIH) sponsored randomized study examining the effects of a prescribed exercise regimen on a group of AAA

patients. In this study, AAA patients are randomized to an exercise or usual-activity control cohort and followed for 3 years.[13]

While gene and protein expression analysis and population based studies provide insight into the inflammatory and peripheral resistance theories of AAA development, the use of noninvasive medical imaging and computational fluid dynamics methods enable an in-depth study of the hemodynamic conditions specific to large arteries, including the abdominal aorta.[55] While important progress has been made in modeling blood flow in arteries over the last decade, much of this work has utilized zero-pressure, or prescribed pressure or flow boundary conditions that result in non-physiologic pressure and/or flow fields. In addition, some studies use severely under-resolved meshes, idealized AAA geometry, or neglect the nearby mesenteric, renal, and iliac arteries that greatly affect the flow entering and exiting the AAA. Additionally, comparatively little progress has been made in using this understanding of hemodynamic mechanisms to guide the development of an effective medical therapy for AAAs.

In this paper, we use magnetic resonance imaging (MRI) and computational fluid dynamics (CFD) to study hemodynamics under rest and exercise conditions in eight AAA patients. The use of MRI provides a means to model blood flow in a highly patient specific manner because it enables the nearly simultaneous acquisition of anatomic and physiologic flow data, whereas the use of computational simulations enable the study of blood flow at resolution many times finer than any imaging modality and can capture transient phenomena unobservable by cardiac-gated imaging sequences. Our hemodynamic analyses include quantification of pressure and velocity, normal stresses in the AAAs, as well as mean wall shear stress (MWSS), oscillatory shear index (OSI), and turbulent kinetic energy (TKE). We aim to quantitatively and qualitatively capture the baseline hemodynamic conditions in AAAs using physiologic boundary conditions, appropriately resolved meshes, and patient-specific geometric models, flow waveforms, and pressures. Additionally, we aim to examine some of the mechanisms by which exercise might slow the growth of AAAs in humans in order to guide and evaluate the effectiveness of exercise as a medical therapy for AAA disease.

Methods

Magnetic Resonance Imaging

Seven male and one female patients with a mean age of 73.3 years (SD: 5.70; range: 66-84) with known small AAAs (<5 cm) were imaged in the supine position using a 1.5T GE Signa MR scanner (GE Medical Systems, Milwaukee WI) with an 8-channel cardiac coil. Imaging studies were conducted under a protocol approved by the institutional review board, informed consent was obtained from all subjects, and all patients were screened for contraindications to MR and gadolinium usage, including renal insufficiency.[60] A 3D gadolinium-enhanced magnetic resonance angiography (MRA) sequence was used to image the lumen of the aorta and nearby branch vessels. Imaging parameters included: 512×192 acquisition matrix (reconstructed to 512×512), a 40 cm^2 square field of view, 3.0-3.3 ms TR (repetition time), 0.7-0.8 ms TE (echo time), and 25° flip angle. A 3-mm slice thickness was used, 124 slices were included in each volume, and all MRAs were acquired coronally. A

cardiac gated 1-component phase contrast sequence (PC-MRI) was used to measure blood flow velocity perpendicular to the aorta at the supraceliac (SC) and infrarenal (IR) levels. Imaging parameters included: 256×192 acquisition matrix (reconstructed to 256×256), a 24×24 to 34×34 cm^2 square field of view, 5 mm slice thickness, 11.9-12.7 ms TR (repetition time), 4.5-5.3 ms TE (echo time), 20° flip angle, and two signal averages. A velocity encoding gradient of 150 cm/s through-plane was used, and 24 time points were reconstructed. The temporal resolution of the velocity data equaled two times the TR (23.8-25.4 ms). Immediately after the MR exam, a brachial systolic blood pressure (SBP) and a diastolic blood pressure (DBP) measurement were acquired using an automatic pressure cuff (Omron Healthcare inc., Bannockburn, Illinois).

Image Processing

First, gradient nonlinearities arising during acquisition were corrected in the MRAs to avoid image distortion in the slice direction of the magnetic field.[14] Next, three-dimensional, patient-specific geometric models were constructed from the MRA data using custom software.[65] The models began at the level of the diaphragm and included the aorta, the hepatic and splenic arteries, the superior mesenteric artery (SMA), the right and left renal arteries, and the right and left internal and external iliac arteries. Approximate centerline paths through the vessels of interest were defined, and the image data were resampled in planes perpendicular to the centerline paths. Vessel boundaries were segmented using a level-set method.[65] Solid models were lofted for each vessel and then unioned to create a single solid model representing the flow domain (Figure 1). A visual comparison between the maximum intensity projections (MIPs) of the MRAs and the 3-D computer models can be seen in Figure 2. For each patient, the PC-MRI images acquired at the SC and IR levels were segmented at each of 24 time-points using a level-set technique, baseline corrected using a linear correction algorithm based on the average background noise, and then assembled into volumetric flow waveforms.

Computational Fluid Dynamics Analysis

The Navier-Stokes and continuity equations representing conservation of momentum and mass of a Newtonian incompressible fluid were used to represent blood flow in an arbitrary numerical domain Ω with boundary Γ. The boundary Γ is such that $\Gamma = \Gamma_i \cup \Gamma_w \cup \Gamma_h; \Gamma_i \cap \Gamma_w \cap \Gamma_h = \varnothing$, where Γ_i represents an inlet boundary where a Dirichlet condition is prescribed on the velocity field; Γ_w represents the vessel wall boundary; and Γ_h represents all the outflow boundaries where a Neumann condition is prescribed. A well-posed Initial Boundary Value Problem is defined by the aforementioned partial differential equations subject to suitable boundary and initial conditions, viz.:

$$\left.\begin{aligned} \rho \vec{u}_{,t} + \rho \vec{u} \cdot \nabla \vec{u} &= -\nabla p + div(\underset{\sim}{\tau}) + \vec{f} \\ div(\vec{u}) &= 0 \end{aligned}\right\} \text{in } \Omega \qquad (1)$$

$$\underset{\sim}{\tau} = 2\mu \underset{\sim}{D} \quad \text{with} \quad \underset{\sim}{D} = \frac{1}{2}\left(\nabla \vec{u} + \nabla \vec{u}^T\right)$$

$$\vec{u}(\vec{x},t) = \vec{u}^{in}(\vec{x},t)\ \vec{x} \in \Gamma_i \quad (2)$$

$$\vec{u}(\vec{x},t) = \vec{0} \quad \vec{x} \in \Gamma_w \quad (3)$$

$$\vec{t}_{\vec{n}}(\vec{x},t) = [-p\underset{\sim}{I} + \underset{\sim}{\tau}]\vec{n} = \vec{h}(\vec{x},t) \quad \vec{x} \in \Gamma_h \quad (4)$$

$$\vec{u}(\vec{x},0) = \vec{u}^{0}(\vec{x}) \quad \vec{x} \in \Omega \quad (5)$$

Here, the primary variables are the blood velocity $\vec{u} = (u_x, u_y, u_z)$ and the pressure p. The blood density ρ and viscosity μ are assumed constant (ρ = 1.06 g/cm^3, μ = 0.04 Poise). The external body force $\vec{f}$ representing gravity was neglected and the vessel wall boundary was assumed to be rigid, as equation (3) indicates. Please note that $\vec{h}$ in equation (4) represents the traction vector imposed on the outflow boundaries Γ_h.

In order to define the variational form corresponding to the equations (1)-(5), we used the following trial solution and weighting function spaces:

$$\begin{aligned} \boldsymbol{S} &= \left\{ \vec{u} \mid \vec{u}(\cdot,t) \in H^1(\Omega)^{n_{sd}}, t \in [0,T], \vec{u}(\cdot,t) = \vec{u}^{in} \text{ on } \Gamma_i, \vec{u}(\cdot,t) = \vec{0} \text{ on } \Gamma_w \right\} \\ \boldsymbol{W} &= \left\{ \vec{w} \mid \vec{w}(\cdot,t) \in H^1(\Omega)^{n_{sd}}, t \in [0,T], \vec{w}(\cdot,t) = \vec{0} \text{ on } \Gamma_i, \vec{w}(\cdot,t) = \vec{0} \text{ on } \Gamma_w \right\} \\ P &= \left\{ p \mid p(\cdot,t) \in H^1(\Omega), t \in [0,T] \right\} \end{aligned} \quad (6)$$

where H^1 represents the usual Sobolev space of functions with square-integrable values and first derivatives in Ω and n_{sd} represents the number of spatial dimensions. Considering this, the variational formulation for this problem can be written as:

$$B_G(\vec{w}, q; \vec{u}, p) = 0$$

$$B_G(\vec{w}, q; \vec{u}, p) = \int_\Omega \left\{ \vec{w} \cdot \left(\rho \vec{u}_{,t} + \rho \vec{u} \cdot \nabla \vec{u} - \vec{f} \right) + \nabla \vec{w} : (-p\underset{\sim}{I} + \underset{\sim}{\tau}) \right\} d\vec{x} - \int_\Omega \nabla q \cdot \vec{u}\, d\vec{x} - \int_{\Gamma_h} \vec{w} \cdot (-p\underset{\sim}{I} + \underset{\sim}{\tau}) \cdot \vec{n}\, ds + \int_\Gamma q \vec{u} \cdot \vec{n}\, ds \tag{7}$$

We adopted the Coupled-Multidomain formulation described in Vignon-Clementel, 2006.[61] This method is based on a variational multiscale decomposition of the domain Ω into an upstream 3D numerical domain $\widehat{\Omega}$ and a downstream reduced-order analytical domain Ω', such that $\widehat{\Omega} \cap \Omega' = \varnothing$ and $\overline{\widehat{\Omega} \cup \Omega'} = \Omega$. The numerical and the analytical domains are separated by an interface Γ_B. This interface is what we refer to as "outlet" or "outlets" (of the 3D computational domain) throughout the paper. Furthermore, the method considers a disjoint decomposition for the flow variables: the solution vector $\vec{V} = \{\vec{u}, p\}^T$ is separated into a component defined within the numerical domain and another component defined within the analytical domain, viz:

$$\vec{V} = \left\{ \widehat{\vec{V}} + \vec{V}' \right\}, \text{ with } \widehat{\vec{V}} \Big|_{\Omega'} = 0 \text{ and } \vec{V}' \Big|_{\widehat{\Omega}} = 0\,. \tag{8}$$

This decomposition satisfies $\widehat{\vec{V}} = \vec{V}'$ at the interface Γ_B, and is also applied to the weighting functions $\vec{w}$ and q. Under these assumptions, equation (7) can be rewritten as:

$$\int_{\widehat{\Omega}} \widehat{\vec{w}} \cdot \left(\rho \widehat{\vec{u}}_{,t} + \rho \widehat{\vec{u}} \cdot \nabla \widehat{\vec{u}} - \vec{f} \right) + \nabla \widehat{\vec{w}} : (-\hat{p}\underset{\sim}{I} + \hat{\underset{\sim}{\tau}}) d\vec{x} - \int_{\hat{\Gamma}_h} \widehat{\vec{w}} \cdot (-\hat{p}\underset{\sim}{I} + \hat{\underset{\sim}{\tau}}) \cdot \widehat{\vec{n}}\, ds + \int_{\Gamma_B} \vec{w}' \cdot (-p'\underset{\sim}{I} + \underset{\sim}{\tau}') \cdot \vec{n}'\, ds - \int_{\widehat{\Omega}} \nabla \hat{q} \cdot \widehat{\vec{u}}\, d\vec{x} + \int_{\hat{\Gamma}} \hat{q} \widehat{\vec{u}} \cdot \widehat{\vec{n}}\, ds - \int_{\Gamma_B} q' \vec{u}' \cdot \vec{n}'\, ds = 0 \tag{9}$$

The integral terms defined on Γ_B represent the continuity of traction and flux at the interface between the numerical and analytical domains. These terms can be approximated by the operators

$$\mathscr{M} = \left\{\underset{\sim}{\mathscr{M}}_m, \vec{\mathscr{M}}_c\right\}\Big|_{\Gamma_B} \quad \text{and} \quad \mathscr{H} = \left\{\underset{\sim}{\mathscr{H}}_m, \vec{\mathscr{H}}_c\right\}\Big|_{\Gamma_B} : \int_{\Gamma_B} \vec{w}' \cdot (-p'\underset{\sim}{I} + \underset{\sim}{\tau}') \cdot \vec{n}'\, ds \tag{10}$$
$$- \int_{\Gamma_B} q'\vec{u}' \cdot \vec{n}'\, ds \approx \int_{\Gamma_B} \vec{w}' \cdot \left(\underset{\sim}{\mathscr{M}}_m(\vec{u}', p') + \underset{\sim}{\mathscr{H}}_m\right) \cdot \vec{n}'\, ds - \int_{\Gamma_B} q'\left(\vec{\mathscr{M}}_c(\vec{u}', p') + \vec{\mathscr{H}}_c\right) \cdot \vec{n}'\, ds$$

The operators $\mathscr{M}$ and $\mathscr{H}$ are defined on the domain Ω' based on the chosen reduced-order model chosen to represent flow and pressure in the downstream domain (i.e., morphometry-based impedance function, lumped-parameter model, etc.). The final weak form of the Coupled-Multidomain method results in:[61]

$$\int_{\hat{\Omega}} \hat{\vec{w}} \cdot \left(\rho \hat{\vec{u}}_{,t} + \rho \hat{\vec{u}} \cdot \nabla \hat{\vec{u}} - \vec{f}\right) + \nabla \hat{\vec{w}} : (-\hat{p}\underset{\sim}{I} + \hat{\underset{\sim}{\tau}}) d\vec{x} - \int_{\hat{\Gamma}_h} \hat{\vec{w}} \cdot (-\hat{p}\underset{\sim}{I} + \hat{\underset{\sim}{\tau}}) \cdot \hat{\vec{n}}\, ds \tag{11}$$
$$- \int_{\Gamma_B} \hat{\vec{w}} \cdot \left(\underset{\sim}{\mathscr{M}}_m\left(\hat{\vec{u}}, \hat{p}\right) + \underset{\sim}{\mathscr{H}}_m\right) \cdot \hat{\vec{n}}\, ds - \int_{\hat{\Omega}} \nabla \hat{q} \cdot \hat{\vec{u}}\, d\vec{x} + \int_{\hat{\Gamma}} \hat{q}\hat{\vec{u}} \cdot \hat{\vec{n}}\, ds$$
$$+ \int_{\Gamma_B} \hat{q}\left(\vec{\mathscr{M}}_c\left(\hat{\vec{u}}, \hat{p}\right) + \vec{\mathscr{H}}_c\right) \cdot \hat{\vec{n}}\, ds = 0$$

Note that the solution in the numerical domain $\hat{\Omega}$ depends on the operators defined by the mathematical model chosen for the downstream analytical domain, expressed as a function of the solution variables of the numerical domain $\left\{\hat{\vec{u}}, \hat{p}\right\}$. For a three-element Windkessel (R_p, C, R_d) model of the downstream vasculature, the operators $\mathscr{M}$ and $\mathscr{H}$ become.[62]

$$\underset{\sim}{\mathscr{M}}_m\left(\hat{\vec{u}}, \hat{p}\right) = R_p \int_{\Gamma_B} \hat{\vec{u}} \cdot \hat{\vec{n}}\, ds + \int_0^t \frac{e^{-\left(t - t_1\right)/\tau}}{C} \int_{\Gamma_B} \hat{\vec{u}}(t_1) \cdot \hat{\vec{n}}\, ds dt_1 + \hat{\vec{n}} \cdot \hat{\underset{\sim}{\tau}} \cdot \hat{\vec{u}} - \hat{\underset{\sim}{\tau}}$$
$$\underset{\sim}{\mathscr{H}}_m = \left(\hat{p}(0) - R_p \int_{\Gamma_B} \hat{\vec{u}}(0) \cdot \hat{\vec{n}}\, d\Gamma - \hat{P}_d(0)\right) e^{-t/\tau} + \hat{P}_d(t) \tag{12}$$
$$\vec{\mathscr{M}}_c\left(\hat{\vec{u}}, \hat{p}\right) = \hat{\vec{u}}$$
$$\vec{\mathscr{H}}_c = \vec{0}$$

where $\tau = R_d C$. Here, R_p represents the proximal resistance, C the capacitance and R_d the distal resistance of the downstream vasculature; P_d is a time-varying function representing the terminal capillary pressure. $P(0)$, $Q(0)$ and $P_d(0)$ are the initial conditions for pressure, flow and capillary pressure for the downstream analytical domain, respectively.

The variational form defined by equations (11) and (12) and the boundary and initial conditions (2)-(5) is then solved using a custom stabilized finite-element solver which

utilizes equal-order interpolation for velocity and pressure.[51,61,64] All simulations were performed using direct numerical simulations, without any assumptions that impose laminar or fully-developed turbulent regimes on the flow. This is justified because most turbulence models assume fully-developed turbulent conditions, which is not the case for pulsatile flow in AAAs: The flow, undoubtedly turbulent during late systole, largely relaminarizes during early systole and diastole.[57] Computations were performed on a 20.6 teraflops super-computer with a total of 2,208 cores (276 Dell PowerEdge 1950 compute nodes, consisting of dual-socket quad-core processors, featuring 16GB of memory each).

Numerical Simulation Details

Below we describe the simulation process for a single patient; the simulation process was repeated in a patient-specific manner for all patients under both rest and exercise conditions. First, the model was discretized into an initial isotropic finite-element mesh with a maximum edge size of 1.5 mm using a commercial meshing kernel (MeshSim™, Simmetrix, Troy, NY). Next, steady simulations with mean SC flow as the inlet boundary condition and resistance outlet boundary conditions were performed on the initial isotropic mesh under both rest and exercise conditions for each patient. Resistances for each outlet were equal to the R_{total} described later. The results of this steady simulation were used to adapt the mesh,[37] creating an average intermediate anisotropic mesh consisting of 922,525 linear tetrahedral elements (SD: 238,766; range 595.558-1,323,275) for rest and 967,862 linear tetrahedral elements (SD: 211,180; range 623,630-1,219,620) for exercise. A pulsatile simulation was then performed on this newly adapted mesh for four cardiac cycles, and the capacitance, C, and R_{total} at each outlet were adjusted slightly as needed to attain mean flows at the outlets and SBP and DBP at the inlet of the model to within 5% of target values. Lastly, a final isotropic mesh with an edge size of 0.5 mm was used for each patient. This resulted in an average mesh size of 9,048,902 linear tetrahedral elements (SD: 2,347,967; range: 5,731,780-11,951,555). Pulsatile simulation were run for eight cardiac cycles using a timestep size of 1/1000th of the cardiac cycle with 5 non-linear iterations per timestep. Thus the mean time step size was 0.000974 seconds (SD: 0.000176; range: 0.000769-0.001333) for rest and 0.000649 seconds (SD: 0.000117; range: 0.000513-0.000889) for exercise. While all 1000 timepoints in each cardiac cycle were solved for, 50 timepoints were written out per cardiac cycle due to data storage constraints. At the time of simulation, the residual for the last iteration of each time step was recorded. The same mesh was used for both rest and exercise. The first three cardiac cycles were ignored, as the pressure waves had not yet achieved periodicity. The fourth through eighth cardiac cycles were used to calculate pressures, velocities, MWSS, OSI, and TKE. For both rest and exercise, outlet velocity profiles were constrained to a parabolic profile using the augmented lagrangian method developed by Kim et al.[28] These constraints were used on an as-needed basis to prevent solution divergence, a common numerical problem when an outlet area experiences reverse or complex flow structures leaving the three-dimensional computational domain. It should be noted that this technique does not affect the *amount* of flow leaving an outlet, but only constrains the shape of the velocity profile at the outlet. Use of constraints on branch vessels of the abdominal aorta has been shown to affect the flow, pressure, MWSS and OSI in the abdominal aorta very little.[28]

Boundary conditions for each patient were derived from literature and from the measured patient-specific SC and IR flows and the measured brachial artery SBP and DBP. At the wall, a no-slip condition was prescribed, as indicated in equation (3). The inlet velocity profile for each patient was defined as follows: A measured (rest) or extrapolated (exercise) SC waveform was decomposed into a steady non-zero mean flow which was mapped to a Poiseuille velocity profile, and a pulsatile zero-mean flow wave which was mapped to a ten-frequency Womersley velocity profile.[66] The Poiseuille and Womersley velocity profiles were then linearly super-imposed to define the inlet velocity profile on Γ_i. At each outlet, a three-element Windkessel model consisting of a proximal resistance (R_p), capacitance (C), and distal resistance (R_d) was used to represent the resistance and capacitance of the proximal vessels (the arteries), and the resistance of the distal vessels (the arterioles and capillaries), downstream of each outlet (Figure 3).[61,62] Below we describe the R_p, C, and R_d specification for a single patient under rest and exercise conditions; this process was repeated in a patient-specific manner for all subjects.

R_p, C, R_d Specification for Rest

Specification of R_p, C, R_d is required for each outlet of the numerical domain in order to fully defined the Coupled-Multidomain analytical representation of the downstream vasculature. The values for these parameters corresponding to resting conditions were chosen using a combination of patient-specific data and literature values as outlined in the following steps:

1. The brachial SBP and DBP acquired immediately after the exam were assumed to be equal to the intraaortic SBP and DBP at the level of the diaphragm, which corresponds to the inlet of our model.[22]
2. Using a three-element Windkessel analog for the system (3D model plus downstream vessels), we determined the total resistance and total capacitance of the system, $R_{total\text{-}system}$ and $C_{total\text{-}system}$, by iteratively solving for a pressure waveform as a function of the input SC flow waveform and the parameters of the Windkessel model. $R_{total\text{-}system}$ and $C_{total\text{-}system}$ were adjusted until the measured SBP and DBP were achieved. In this process, we assumed a $R_{p\ total\text{-}system}/R_{total\text{-}system}$ ratio of 5.6%.[30] The mean blood pressure was calculated as $R_{total\text{-}system}$ times mean SC flow. This is similar to the method used by Stergiopolus and colleagues with a two-element Windkessel model.[52]
3. The target mean flows to each outlet were calculated as follows: Target mean upper branch vessel flows (UBVF) were determined by subtracting the mean measured IR flow from the mean measured SC flow and then distributing this UBVF based on literature: 33.0% to the celiac (which was then distributed 50% to the hepatic and 50% to the splenic arteries), and 22.3% to the SMA, the left renal artery, and the right renal artery.[35] In the presence of accessory renal arteries, renal flow was divided proportional to outlet area.
4. The mean IR flow was divided equally to the two common iliac arteries; 70% of this flow was diverted to the external iliac arteries and 30% was assigned to the internal iliac arteries, thus providing the target mean flow to each iliac artery.[51]

5. The total resistance ($R_{total}=R_p + R_d$) at each outlet was calculated as mean blood pressure divided by target mean flow at each outlet. For the purposes of estimating the initial R_{total} value, we assumed that the mean pressure at the inlet of the model was equal to the mean pressure at the outlets.

6. Except for the renal arteries, the proximal resistance, R_p, for each outlet was arbitrarily chosen to be 5.6% of R_{total}.[30] For the renal arteries, R_p was arbitrarily chosen to be 28% of R_{total} to account for the unique features of renal flow: an absence of backflow throughout the cardiac cycle and relatively high and constant diastolic flow.[3,21] These flow features result from the relatively low resistance of the distal vascular beds of the kidneys,[41] a feature captured in the comparatively low R_d value assigned to the renal arteries.

7. Lastly, capacitance, C, for each outlet was calculated by distributing the $C_{total\text{-}system}$ proportional to flow at each outlet.

R_p, C, R_d Specification for Exercise

Resting waveforms, target SBP and DBP, target mean flows, and the R_p, C, R_d values were altered in accordance with literature to simulate moderate lower-limb exercise.

1. Each patient was categorized as hypertensive or normotensive, and a target exercise SBP and DBP were calculated for a 50% increase in heart rate by linearly interpolating the hypertensive and normotensive data from Montain et al.[34]

2. The target mean resting IR flow was increased 5.44-fold, in accordance with in vivo measurements by Cheng et al.[10] and target mean exercise UBVF were calculated by decreasing the total flow to each upper branch vessel 21% from rest. This is in agreement with Cheng et al.[10] and the assumption that flow to the renal, celiac, and mesenteric system decreases with moderate lower-limb exercise as a result of the vasoconstriction of these vascular beds during exercise.

3. The target mean exercise IR flow and the target mean exercise UBVF were summed to generate a target mean exercise SC flow. Because each patient had a slightly different measured mean resting SC/IR flow ratio, the calculated target mean exercise SC flow increased an average of 2.57-fold (SD: 0.41; range: 1.90-3.07) from rest to exercise, similar to the 2.61-fold SC increase found in Cheng et al.[10]

4. The diastolic portion of the resting SC flow waveform was truncated such that heart rate increased 50%,[10] and the remaining flow waveform was shifted up to match the target mean exercise SC flow. Thus, the resulting exercise SC waveform lacked diastolic backflow and the systolic portion of the waveform represented a greater portion of the cardiac cycle, a result similar to experimental measurements.[10]

5. This extrapolated patient-specific exercise SC waveform was mapped to the inflow face of the model using a Womersley velocity profile.

6. Similar to rest, a three-element Windkessel analog for the system under exercise conditions (3D model plus downstream vessels) was used to determine the total resistance and total capacitance of the system, $R_{total\text{-}system}$ and $C_{total\text{-}system}$, by iteratively solving for a pressure waveform as a function of the input extrapolated SC flow waveform and the parameters of the Windkessel model. $R_{total\text{-}system}$ and $C_{total\text{-}system}$ were adjusted until the measured SBP and DBP were achieved. In this process, we assumed a $R_{p\ total\text{-}system}/ R_{total\text{-}system}$ ratio of 5.6%. The mean blood pressure was calculated as $R_{total\text{-}system}$ times target mean SC exercise flow.

7. Using the target exercise pressures and mean flows, the resting $R_{p,}$ C, R_d parameters were altered to simulate exercise. First, R_{total} was calculated for each outlet as the mean pressure divided by the target mean exercise flow for each branch vessel.

8. R_p was kept the same as rest; as the arteries just distal to the outlets of the model were assumed to neither dilate nor constrict significantly during exercise.

9. R_d was calculated as R_{total} minus R_p. Thus, R_d reflected the physiologic states of the distal vascular beds during lower-limb exercise: R_d increased in the upper branch vessels during exercise, reflecting the vasoconstriction of the arterioles and capillaries in celiac, mesenteric and renal systems during exercise, while R_d dramatically decreased in the iliac arteries,[21] reflecting the vasodilation of arterioles and recruitment of the capillaries during exercise. This unchanging R_p and dramatically reduced R_d during exercise is supported by experimental data reported by Laskey and colleagues.[30]

10. Similar to the rest case, the total capacitance, $C_{total\text{-}system}$, was distributed proportional to flow at each outlet.

Dimensionless Variables Governing Flow

The mean and systolic Reynolds numbers and the Womersley numbers were calculated from the SC and IR phase contrast data as follows:

$$\text{Reynolds}_{\text{mean}} = \frac{\rho 4 Q_{mean}}{\pi D_{mean} \mu} \quad (13)$$

$$\text{Reynolds}_{systole} = \frac{\rho 4 Q_{systole}}{\pi D_{mean} \mu} \quad (14)$$

$$Womersley\ Number = R\left(\frac{\omega \rho}{\mu}\right)^{\frac{1}{2}} \quad (15)$$

where Q_{mean} is the mean flow over the cardiac cycle, $Q_{systole}$ is the systolic (peak) flow over the cardiac cycle, D_{mean} is the mean diameter of the aorta at the SC or IR location, μ is the dynamic viscosity of 0.04 Poise, ρ is the density (1.06 g/cm^3), and ω is the angular frequency (equal to 1/cardiac cycle length).

Normal Stresses

The distribution of normal stresses (including both the static and dynamic viscous components) acting on the aneurysm lumen at peak flow was plotted for all eight patients for rest and exercise. We described the temporal and spatial variation of the total normal stress acting on the aneurysm luminal wall: First, we calculated the spatial range of the normal stress at peak flow for both rest and exercise. Then, we computed the temporal range of the normal stresses by subtracting the maximum and minimum average normal stresses in the aneurysm over the cardiac cycle for both rest and exercise. Last, we calculated the ratio between the spatial and temporal ranges of the total normal stress for all eight patients during rest and exercise. The time points corresponding to peak flow and maximum normal stresses in the aneurysms were not necessarily the same, as pressure generally lags flow.

Shear Stress

MWSS and OSI were averaged over the fourth through eighth cardiac cycles and then quantified in one-centimeter strips at four aortic locations: One cm above the celiac artery (supraceliac, SC), one centimeter below the most distal renal artery (infrarenal, IR), at the largest diameter of the aneurysm (Mid-An), and one centimeter above the aortic bifurcation (suprabifurcation, SB). When averaging over the fourth through eighth cardiac cycles, the MWSS, $\vec{\tau}_{mean}$, was defined as:

$$\vec{\tau}_{mean} = \left| \frac{1}{5T} \int_{3T}^{8T} \vec{t}_s dt \right|. \quad (16)$$

Here, T is the period of one cardiac cycle, $\vec{t}_s$ is the wall shear vector defined as the in-plane component of the surface traction vector $\vec{t}$ $\left(\text{i.e., } \vec{t}_s = \vec{t} - \left(\vec{t} \cdot \vec{n}\right)\vec{n}\right)$. The surface traction vector $\vec{t}$. The surface traction vector $\vec{t}$ is calculated solving a new variational problem where the solution for velocity and pressure is known, and the goal is to evaluate the traction at the boundaries of the domain. This approach is known as *variationally consistent* calculation of boundary fluxes.[24] When averaging over the fourth through eighth cardiac cycles, OSI, which measures the unidirectionality of shear stress, was calculated as:

$$OSI = \frac{1}{2}\left(1 - \frac{\left| \frac{1}{5T}\int_{3T}^{8T} \vec{t}_s dt \right|}{\frac{1}{5T}\int_{3T}^{8T} \left| \vec{t}_s \right| dt}\right) \quad (17)$$

where T is again the period of one cardiac cycle and t_s is the in-plane component of the surface traction vector. OSI values range from 0 to 0.5, where 0 indicates unidirectional shear stress, and 0.5 indicates shear stress with a time-average of zero.[20,56]

Turbulent Kinetic Energy

In order to study turbulence in the AAA models, we investigated the cycle-to-cycle variation of the velocity field by computing the turbulent kinetic energy (TKE). A brief summary of the derivation of TKE is shown below.

The TKE computation is centered upon a decomposition of the velocity field $\vec{u}(\vec{x},t)$ into an averaged part $\vec{U}(\vec{x},t)$ plus a fluctuating part $\tilde{\vec{u}}(\vec{x},t)$. First, we assume that the velocity field, $\vec{u}(\vec{x},t)$, is nominally periodic with respect to the cardiac cycle, where $\vec{x}$ denotes space and t denotes time. Next, an ensemble average is computed by averaging out the cycle-to-cycle changes in n cardiac cycles worth of data and mapping them to a single cardiac cycle. Mathematically, given n cardiac cycles of the velocity field $\vec{u}(\vec{x},t)$ where $t\in[0,nT)$, we define the ensemble average $\langle\vec{u}\rangle(\vec{x},s)$ as:

$$\langle\vec{u}\rangle(\vec{x},s)=\frac{1}{n}\sum_{k=0}^{n-1}\vec{u}(\vec{x},s+kT),\quad \forall\,\tau\in[0,T).\qquad(18)$$

This ensemble average is then extended over n cardiac cycles to cover the same temporal domain as the original velocity field $\vec{u}(\vec{x},t)$. This extension is accomplished by repeating $\langle\vec{u}\rangle(\vec{x},s)$ n times to generate the periodic average $\vec{U}(\vec{x},t)$. Mathematically,

$$\vec{U}(\vec{x},t)=\langle\vec{u}\rangle(\vec{x},t\ \text{modulo}\ T),\qquad(19)$$

where t modulo T gives the remainder when t is divided by T. Now, the fluctuation velocity field can be defined by subtracting the periodic average from the original velocity field:

$$\tilde{\vec{u}}(\vec{x},t)=\vec{u}(\vec{x},t)-\vec{U}(\vec{x},t).\qquad(20)$$

Finally, the mean fluctuating kinetic energy per unit mass, often referred to as the *turbulent kinetic energy*, is defined as:

$$k(\vec{x}\,.s)=\frac{1}{2}\rho\left[\left\langle\tilde{\vec{u}}_1^2\right\rangle(\vec{x},s)+\left\langle\tilde{\vec{u}}_2^2\right\rangle(\vec{x},s)+\left\langle\tilde{\vec{u}}_3^2\right\rangle(\vec{x},s)\right],\quad\forall\,\tau\in[0,T),\qquad(21)$$

where the density, ρ is 1.06 g/cm^3 and $\tilde{u}_i$ denotes the i$^{\text{th}}$ component of $\tilde{u}$, and

$$\left\langle \tilde{u}_i^2 \right\rangle (x,s) = \frac{1}{n}\sum_{k=0}^{n-1} \tilde{u}_i^2(x, s+kT), \quad \forall\ \tau \in [0,T)\,. \quad (22)$$

Similarly, the ensemble-averaged kinetic energy, KE, was defined as:

$$k(\vec{x},s) = \frac{1}{2}\rho\left[\left\langle \vec{u}_1^{\,2}\right\rangle(\vec{x},s) + \left\langle \vec{u}_2^{\,2}\right\rangle(\vec{x},s) + \left\langle \vec{u}_3^{\,2}\right\rangle(\vec{x},s)\right], \quad \forall\ \tau \in [0,T) \quad (23)$$

where the density, ρ is 1.06 g/cm^3 and u_i denotes the ith component of u, and

$$\left\langle \vec{u}_i^{\,2}\right\rangle(\vec{x},s) = \frac{1}{n}\sum_{k=0}^{n-1} \vec{u}_i^{\,2}(\vec{x}, s+kT), \quad \forall\ \tau \in [0,T) \quad (24)$$

To quantify the TKE and kinetic energy (KE) within the abdominal aorta and aneurysm, the abdominal aorta was first isolated by trimming the model superiorly just distal to the lowest renal artery and inferiorly just proximal to the aortic bifurcation. The mean TKE and KE at peak systole, mid-deceleration, and mid-diastole were quantified over cardiac cycles 4 though 8 on the final meshes for all eight patients during both rest and exercise.

Mesh and Temporal Independence Study

In order to ensure the mesh-independence of our solutions, three isotropic meshes consisting of 2,175,303 (edge size: 0.82 mm), 8,343,663 (edge size of 0.5 mm), and 31,831,619 linear tetrahedral elements (edge size 0.3 mm) were generated for patient 1 (Figure 4). Hereafter, these meshes will be abbreviated as the 2.2, 8.3, and 31.8-million element meshes. These meshes were chosen such that ratio of element from the small to intermediate and intermediate to large meshes would be approximately the same. Simulations were performed for eight cardiac cycles using the same patient-specific exercise boundary conditions. The resultant instantaneous velocity field and MWSS and OSI values were compared. Additionally, to ensure the temporal independence of our solutions, the patient 1 exercise simulation on the final mesh (8.3-million elements) was extended for an additional five cardiac cycles. The resultant MWSS, OSI, and TKE calculated from cardiac cycles four through eight were compared to those calculated from cardiac cycles nine through thirteen.

Comparison of Measured and Simulated Infrarenal Flow Waveforms

The measured and simulated IR flow waveform were compared. The simulated IR waveforms resulted purely from the inlet SC waveforms and the outlet boundary conditions; the shape of the IR waveforms were never prescribed or specified in the simulation process, and thus the IR waveforms provided a good measure of how well simulated flow conditions matched the measured flow conditions for each patient.

Results

Morphology of AAAs

The MRAs showed that AAA luminal morphology varied widely from patient to patient, with shapes varying from fusiform (patients 1, 4, and 5), single-lobed (patients 2, and 7), and bi-lobed (patients 3, 6, and 8) (Figure 2).

Measured Flows and Pressures

The mean flow measured from the PC-MRI scans were 3.51 L/min (SD: 0.50; range: 2.51-4.32) for SC and 1.31 L/min (SD: 0.34; range: 0.84-1.75) for IR. The mean measured SBP was 155.8 mmHg (SD: 12.2; range: 136-170) and the mean measured DBP was 90.9 mmHg (SD: 6.8, range: 80-100), indicating the presence of hypertension.

Simulation

For the final finite element meshes, the mean absolute residual for cycles four through eight was 2.9e-4 (SD: 1.7e-4, range: 1.0e-5 - 6.0-e4) under resting conditions and 1.8e-3 (SD: 1.2e-3; range: 1.5e-4 - 3.7e-3) under exercise conditions. For the mesh independence study the average absolute residual was 4.6e-3 for the 2.2-million element mesh, 2.3e-3 for the 8.3-million element mesh, and 7.1e-4 for the 31.8 million element mesh. For the temporal independence study of patient 1 under exercise conditions, the mean residual was 2.3e-4 for both cardiac cycles four through eight and cardiac cycles nine through thirteen. For each of the 16 simulations (eight patients, rest and exercise conditions), the boundary condition tuning process took approximately one week, and the final simulation took approximately three to seven days, using 96 cores per day. For the mesh independence study, the largest mesh (32.6M elements) took approximately one week using 200 cores per day.

Simulated Flows, Pressures, and Velocities

All simulated mean flows were within 5% of target mean flows. In addition, all resting inlet SBPs and DBPs (pressures averaged over the inlet area) were within 5% of measured brachial SBPs and DBPs, and all exercise inlet SBP and DBP were within 5% of target pressures. Furthermore, the resting renal volumetric flow remained antegrade throughout the cardiac cycle in accordance with literature,[3] and retrograde flow was decreased or eliminated in the iliacs during exercise for all eight patients, resulting in a “vasodilation” impedance spectra for the iliac arteries during exercise. These features are evident in the inlet and selected outlet pressure and flow waveforms for patient 3 under rest and exercise conditions shown in Figure 5. The magnitude of the ensemble-average of the velocity, $\|\langle\vec{u}\rangle(\vec{x},s)\|$, calculated from cardiac cycles four through eight at peak systole, mid-deceleration, and mid-diastole were plotted for all eight patients using volume-rendering techniques to highlight features in the flow stream Figure 6. The peak systolic, mid-deceleration, and mid-diastolic times varied from patient to patient, due to differences in heart rate and waveform shape. The peak systolic, mid-deceleration, and mid-diastolic times varied from patient to patient, due to differences in heart rate and waveform shape. We defined “peak systole” as the point in time corresponding to the largest SC flow; “mid-deceleration” as the point in time mid-way between maximum SC flow and minimum (usually flow reversal) SC flow; and “mid-

diastole" as the point in time approximately 80% through the completion of cardiac cycle. The magnitude of ensemble-average velocity showed highly complex flow features, especially during mid-deceleration and mid-diastole.

Dimensionless Variables Governing Flow

The mean and systolic Reynolds numbers as well as the Womersley number can be seen in Table 1. The mean Reynolds numbers at the SC and IR location were relatively low, while peak Reynolds numbers were 3-5 times higher. The Womersley numbers at the SC and IR location were 6.45 and 5.87, respectively.

Normal Stresses

The distribution of normal stresses acting on the aneurysm wall at peak flow for all eight patients during rest and exercise is shown in Figure 7. Table 2 summarizes the spatial variation of normal stress (at peak flow), and the temporal variations (over the cardiac cycle), and their ratio. The spatial variations of normal stresses at peak flow were generally small during rest (mean 2.10; SD: 1.99; range: 0.46-6.67 mmHg) and larger during exercise (mean 7.89; SD: 5.68; range: 1.11-18.3 mmHg). The spatial variations were generally a small percentage of the temporal variations of normal stress in the aneurysms over the cardiac cycle. For rest, the ratio of the spatial to temporal variations of normal stresses had an average value of 3.72% (SD: 4.64; range: 0.64-14.9%). During exercise, this ratio had an average value of 8.98% (SD: 7.51; range: 1.17-25.1 %) of the temporal variation.

Mean Wall Shear Stress and Oscillatory Shear Index

The following MWSS and OSI results were calculated from the eight AAA patients at rest and exercise on their final meshes (an average of 9,048,902 linear tetrahedral elements; SD: 2,347,967; range: 5,731,780-11,951,555). MWSS during rest was 3.6 dynes/cm^2 at the SC location (SD: 1.3; range 2.2-5.6), 4.7 dynes/cm^2 at the IR location (SD: 2.6; range 1.6-10.2), 2.5 dynes/cm^2 at the Mid-An location (SD: 2.1; range: 0.9-6.5), and 7.3 dynes/cm^2 at the SB location (SD: 5.1; range: 0.6-16.9). MWSS increased to 9.2 dynes/cm^2 at the SC location (SD: 4.5; range: 4.7-18.0), 33.0 dynes/cm^2 at the IR location (SD: 23.5; range: 5.3-83.7), 21.7 dynes/cm^2 at the Mid-An location (SD: 14.6; range: 7.5-52.3), and 63.8 dynes/cm^2 at the SB location (SD: 40.3; range: 5.2-121.6) during exercise. The rest-to-exercise changes in MWSS at each location were statistically significant ($p=0.0025$, 0.0065, 0.0036, 0.0028, respectively, for rest-to-exercise changes at the SC, IR, Mid-An, and SB locations). In comparing MWSS at different aortic locations under resting conditions, the only sites that were statistically different were IR versus Mid-An ($p=0.017$) and Mid-An versus SB ($p=0.020$). In comparing MWSS at different aortic locations under exercise conditions, MWSS was statistically different for SC versus IR ($p=0.025$), SC versus Mid-An ($p=0.021$), SC versus SB ($p=0.0044$), IR versus SB ($p=0.042$), and Mid-An versus SB ($p=0.040$). The OSI values during rest were 0.28 at the SC location (SD: 0.06; range: 0.19-0.35), 0.24 at the IR location (SD: 0.05; range: 0.16-0.30), 0.27 at the Mid-An location, (SD: 0.06; range: 0.17-0.33), and 0.19 at the SB location (SD: 0.08; range: 0.10-0.36). The OSI decreased at all five locations during exercise. The mean OSI values during exercise were 0.18 at the SC location (SD: 0.08; range 0.08-0.30), 0.10 at the IR location (SD: 0.07; range 0.001-0.23), 0.21 at the Mid-An location (SD: 0.04; range 0.15-0.29), and 0.11 at the SB location (SD:

0.06; range: 0.03-0.20). The rest-to-exercise changes in OSI at each location were statistically significant (p=0.000087, 0.00012, 0.0090, 0.0024, respectively, for rest-to-exercise changes at the SC, IR, Mid-An, and SB locations). Resting OSI was only statistically different for SC versus SB (p=0.023), while exercise OSI values were statistically different for SC versus IR (p=0.0018), SC versus SB (p=0.023), IR versus Mid-An (p=0.0011), and Mid-An versus SB (p=0.0033). MWSS and OSI plots for all eight patients are shown in Figure 8 and Figure 9 and quantitative results are shown in Figure 10 at SC, IR, Mid-An and SB locations.

Turbulent Kinetic Energy

TKE was plotted at peak systole, mid-deceleration, and mid-diastole for all eight patients (Figure 11). Volume rendering techniques were used to display these results through the flow stream. Except for patient 8, the TKE in the aorta for all patients was virtually zero superior to the aneurysm, suggesting that the AAA itself introduces or amplifies turbulence. Qualitatively, some turbulence was observed at rest, agreeing with experimental measurements.[42] For all patients, TKE increased drastically during exercise, with the greatest TKE at mid-deceleration. The presence of TKE in mid-diastole, when flow is low, suggests that instability introduced during systole propagates to diastole.

The mean TKE, mean KE, and TKE/KE ratio values within the abdominal aorta and aneurysms of all eight patients at three points in the cardiac cycle during rest and exercise can be seen in Table 3. The TKE during rest was relatively mild (TKE<100 g cm/s^2), while the TKE during exercise was in the mild to moderate range (TKE range: 5.89-410.78 g cm/s^2). During rest, TKE was lowest at peak systole and had a mean value of 1.84 g cm/s^2 (stdev: 1.32; range: 0.51-3.79), indicating very low turbulence and likely laminar flow. TKE was highest at mid-deceleration for both rest (mean: 7.45 g cm/s^2; stdev: 10.90; range: 0.60-30.62) and exercise (mean: 170.19 g cm/s^2; stdev: 167.22; range: 5.89-410.78). For both rest and exercise, the range in TKE values between patients was quite large, resulting in large standard deviations. There appeared to be a relationship between aneurysm type and TKE. The patients with the most pronounced bi-lobed AAAs, patients 6 and 8, consistently had the highest TKE values for all three points in the cardiac cycle during both rest and exercise. Patient 3, with a more subtle bi-lobed aneurysm also tended to have higher TKE values.

Not surprisingly, the TKE and KE increased from rest to exercise at peak-systole, mid-deceleration, and mid-diastole. However, while the rest-to-exercise TKE changes were not statistically significant at peak systole (p<0.09); they were statistically significant at mid-deceleration (p<0.05) and mid-diastole (p<0.05). Rest-to-exercise changes in KE were statistically significant at peak systole (p<0.001), mid-deceleration (p<0.001), mid-diastole (p<0.01). The ratio of TKE/KE was highest during diastole for all patients for both rest and exercise (except for patient 3 during exercise). However, this high ratio results from the relatively low KE during diastole.

Mesh and Temporal Independence Study

Cut-planes of instantaneous velocity magnitudes at the suprarenal and mid-aneurysm locations are shown at peak systole, mid-deceleration, and mid-diastole for the 2.2, 8.3, and 31.8-million element meshes in Figure 12. The velocities shown are for the eighth cardiac cycle for patient 1 under exercise conditions. Here, it is evident that in regions of zero or near-zero TKE (see Figure 11), such as the suprarenal region, the velocity field changes little between meshes. However, in regions of high TKE, such as the mid-aneurysm location, mesh independence of instantaneous velocity fields is unlikely.

The resultant MWSS and OSI for the three meshes for patient 1 during exercise are shown in Figure 13. The MWSS decreased as the number of elements in the mesh increased, suggesting that finer meshes resolve the low flow or flow stagnation near the wall better than coarser meshes. The maximum MWSS difference between the 2.2 and 8.3-million element meshes, and the between 8.3-million and 31.8-million element meshes were 28.3% and 8.4%, respectively, both at the SB level. OSI changed less predictably between meshes, with maximum OSI differences between the 2.2-million and 8.3-million element meshes, and between the 8.3-million and 31.8-million element meshes of 21.0% and 27.6%, respectively, both at the SB level. These results suggest that the solution derived from 8.3-million elements does not represent a mesh-independent solution for OSI. However, we determined that it was not feasible in terms of time or data storage to run all our simulations on the order of 30-million elements, so we settled on using meshes on the order of 9-million elements (generated with a max edge size 0.5 mm, as described in the methods section) for all our final simulations. These final meshes contain an order of magnitude more elements than the meshes used in previous studies.[16,53]

Our temporal independence study showed promising results; the differences between MWSS and OSI calculated from cardiac cycles four through eight compared to cardiac cycles nine through thirteen were 0.14%, 0.09%, 2.74%, and 0.60% for MWSS and 0.20%, 2.03%, 2.15%, 0.92% for OSI at the SC, IR, Mid-An, and SB levels, respectively. Qualitatively, the TKE varied little when calculated from cardiac cycles four through eight compared to cardiac cycles nine through thirteen. We thus concluded that quantifying MWSS, OSI, and TKE from cardiac cycles four through eight was appropriate.

Comparison of Measured and Simulated Infrarenal Flow Waveforms

In general, the shape of the simulated and measured IR volumetric flow waveforms agreed well and the simulated and measured mean IR flows differed by an average of 0.34% (SD: 0.411%; range: 0.00621%-1.28%). However, the simulated IR waveforms underestimated max and min flow, with simulated $flow_{max}$-$flow_{min}$ differing an average of 18.1% (SD: 10.9%; range: −1.75% to −32.6%) compared to the measured $flow_{max}$-$flow_{min}$. The comparison between measured and simulated infrarenal waveforms can be seen in Figure 14.

Discussion

These results demonstrate, for the first time, three-dimensional patterns of blood flow at rest and exercise for eight AAA patients using patient-specific models, volumetric flow

waveforms, and pressures and highly refined finite-element meshes. Using three-element Windkessel boundary conditions, we were able to achieve flow and pressure features that would have been unattainable with zero-pressure outlet boundary conditions. These unique features include physiologic pressures at the inlet and outlets, always-antegrade renal flow, as well as a vasodilation impedance spectra in the iliacs during exercise. In addition, the use of a 3-element Windkessel (R_p, C, R_d) boundary condition formulation does not make any assumptions about flow periodicity, unlike impedance boundary conditions, and thus may enable a more appropriate computation of turbulence. While our solutions may not have achieved perfect mesh independence, we report results on meshes an order of magnitude or more greater than previous studies.[16,53] Also for the first time, we present mean wall shear stress and oscillatory shear index averaged over multiple cardiac cycles at four discrete locations for both rest and exercise, and we present qualitative and quantitative turbulent kinetic energy for both rest and exercise. Lastly, we report the spatial and temporal ranges of normal stresses on the luminal wall of the AAAs.

Morphology, Flows and Pressures

The morphology of the AAAs varied widely from patient to patient. It is important to note that none of the aneurysms we present were similar to the “textbook” balloon shape frequently seen in studies of idealized AAAs. The mean measured SC and IR flows were greater than those found in Cheng et al., but we report a similar average SC to average IR flow ratio: 2.68 for our patients compared to 2.56 for Cheng et al. The increased SC and IR flows may reflect the relatively high weight (201.5±16.2 lbs) of our patients. The flow was found to be extremely complex with vortices forming and dissipating quickly; thus the vortices observed throughout the cardiac cycle in idealized AAA models may not be realistic.[58] The slightly high SBPs and DBPs are similar to measurements reported in other papers,[32] and may reflect the hypertension commonly found in AAA patients.

Dimensionless Variables Governing the Flow

Our reported Reynolds numbers are useful for comparing to other studies and giving a global idea of turbulence, however, comparing these results to the threshold for turbulence in a straight tube under steady flow conditions (2300) is not advised, as the geometry of the aneurysms and transient nature of arterial blood flow are very different from those present in steady flow in a straight tube.

Normal Stresses

In most cases, the ratio of spatial to temporal normal stresses in the aneurysm was small (averages of 3.72% and 8.98% during rest and exercise, respectively). However, in some patients such as patient 8, the ratio was significantly larger (14.9% and 25.1% during rest and exercise, respectively). These large spatial variations result from the large pressure gradients required to drive flow through the aneurysm at peak systole. These results highlight the importance of incorporating the pulsatility of blood flow when examining normal stresses acting on the aneurysmal lumen wall. Furthermore, these results may have important implications for the design of computational studies investigating the distribution of aneurysm vessel wall stresses. These studies typically consider a hydrostatic pressure field acting as a load on the aneurysm lumen. However, as observed in Figure 7 and Table 2,

the spatial gradients of the loads may be very significant. Therefore, when performing analysis of aneurysm vessel wall stresses, a coupled fluid-structure-interaction simulation of blood flow and wall dynamics may be required in order to capture the spatial heterogeneity of the blood flow normal stresses acting on the aneurysm lumen.

Mean Wall Shear Stress

Our MWSS values were slightly lower than the MWSS found in young, healthy abdominal aortas by Tang and colleagues at the SC, IR, and SB locations under resting conditions (SC, 8.4 dynes/cm^2; IR, 5.1 dynes/cm^2; SB 5.1 dynes/cm^2) and at the IR location during exercise (SC, 33.3 dynes/cm^2).[53] It is possible that our lower shear values reflect the normal dilation of the abdominal aorta (apart from aneurysm dilation) that occurs with age, or could result from the fact that the meshes in these two studies differ by more than an order of magnitude. The MWSS reported at the SC and SB locations in the same study (SC, 20.2 dynes/cm^2; SB, 33.2 dynes/cm^2) locations under exercise conditions was higher, and lower, respectively than our values.[53] The increased MWSS we observed at the SB location probably results from flow impingement on the aortic wall after exiting the AAA. Our MWSS values were also consistently higher than the MWSS in older, healthy aortas during rest and exercise measured directly from MRI (SC: rest 2.3 dynes/cm^2, exercise 6.0 dynes/cm^2; IR: rest 0.9 dynes/cm^2, exercise 4.9 dynes/cm^2).[10] This difference could result from the low spatial resolution of the MR techniques used to measure MWSS. The increased shear stress we found at the distal (SB) location compared the proximal (IR) and mid-aneurysm locations during both rest and exercise agrees with previously published results.[4,26] Lastly, our mid-aneurysm MWSS values also agreed well with the magnitude of shear stress measured in the aneurysm region (1-2 dynes/cm^2) at different points in the cardiac cycle reported by Peattie and colleagues.[42] Because low wall shear stress is thought to correlate with atherosclerosis and perhaps aneurysm growth, we think that the increased MWSS seen during exercise may ultimately reduce vessel wall degeneration and/or attenuate AAA growth.

Oscillatory Shear Index

OSI is an important measure of hemodynamic forces acting on the wall, but unfortunately, is not often reported in the literature. Several studies have reported highly oscillatory flow within AAAs, but include a small sample size, or fail to report average values within the AAA and the proximal or distal aorta.[47,48] Our OSI values were similar to those found computationally in healthy, young abdominal aortas by Tang and colleagues at the IR and SB locations during rest (IR, 0.23; SB 0.20), but the OSI value we found at the SC location was higher than the values they found at the SC location (0.14). It is possible that our increased OSI value at the SC location results from the fact that our fine meshes could resolve oscillatory flow inherent in the Womersley velocity profile–which is prescribed just proximal to the SC location–better than the coarser meshes of previous studies. During exercise, our OSI values were consistently higher than those reported in young, healthy abdominal aortas (SC, 0.06; IR, 0.07; SB, 0.02). This difference could result from our increased mesh resolution, or from the fact that the flow in the aneurysmal abdominal aorta is more complex and recirculating than the flow during exercise in the young, healthy abdominal aorta. Our OSI values were similar to those found from imaging data in healthy, older abdominal aortas at the IR level during rest (0.25), but our values were significantly

higher than the values reported at the SC levels during rest (0.07) and at the SC and IR levels during exercise (SC, 0.0; IR 0.0).[10] These differences may result from the limited spatial resolution of the MR technique used to measure the OSI.

Turbulent Kinetic Energy

We found mild turbulence at rest and moderate turbulence during exercise, with turbulence occurring throughout the AAA. These results concur with some observations from experiments using idealized models of AAAs of varying diameters: Peattie et al. reported increased instability with increased aneurysm size and increased instability in the distal end of the AAA.[42] Egelhoff et al. found attached flow during resting conditions in small AAAs, vortex formation and translation under resting conditions for moderate AAAs, and turbulence under exercise conditions in moderate AAAs.[15] Salsac and colleagues also reported attached flow during systole but transition to turbulent flow during diastole under resting conditions.[48] Turbulence has also been reported in AAA with the use of ultrasound.[6] While some authors report that turbulence significantly increases pressure,[26,27] the actual change in wall pressure from laminar to turbulent flows in these studies is on the order of a few mmHg,[26] and thus we believe it is not a safety concern for exercising patients. Because flow stasis or near-stasis is thought to correlate with thrombus development,[48] we think that the moderate turbulence seen during exercise may reduce areas of flow stasis and thus restrict the growth of thrombus within AAAs.

Our results suggest that turbulence is zero or virtually zero superior to the AAA and that turbulence is likely introduced or amplified by the aneurysm. However, because we prescribe a laminar, periodic flow at the inlet (well above the celiac artery), it is possible that this prescription prevents us from observing turbulent flow superior to the AAA in silico, as the flow does not have sufficient space to develop aperiodicity. Because phase-contrast MRI cannot measure the cycle-to-cycle variation in velocity (k-space is filled over many cardiac cycles), a different flow measuring technique that does not assume periodicity would be required to investigate the impact of the inlet condition on the appearance of flow instabilities in the computational domain. One such technique would be ultrasound. In addition, an evaluation of turbulent kinetic energy in a computational model of an AAA that extends from the heart to the iliac arteries would be worthwhile to study turbulence in the infrarenal aorta, because the arbitrary, laminar and periodic inlet condition would be much further away from the region of interest. Furthermore, while we cannot guarantee that the flow is periodic at the supraceliac level in vivo, we feel that our models represent a drastic improvement upon models that begin infrarenally, yet purport to study turbulence: The model inlet–where laminar, periodic flow is typically prescribed–should never be just proximal to a region known to introduce or amplify turbulence–such as an aneurysm–because this prescribed flow may make the flow more periodic (and less turbulent) in the region of interest.

The quantitative TKE results show that turbulence is relatively mild during rest, and in the mild-to-moderate range during exercise. The elevated TKE values at mid-deceleration suggest that deceleration introduces flow instabilities. This elevated TKE during deceleration agrees with the S.I. Sergeev's seminal studies of oscillatory flow in a pipe,[50]

which found elevated turbulence during deceleration. Turbulence intensity (TI) is another measure of turbulence that is roughly equal to the square root of TKE/KE. Considering this relationship, our approximate TI values during deceleration agree with other in-vitro studies of flow in AAAs under steady inflow conditions.[2] Normalization of the TKE value by the KE value enables a comparison between patients and within cardiac cycles, however, this normalization may overemphasize the importance of turbulence when the kinetic energy is low, for example, during diastole.

Despite moderate turbulence during deceleration, we do not expect this level of turbulence to induce hemolysis. A commonly cited threshold for hemolysis is 400 N/m^2.[46] In cgs units, this is 4000 g $cm^{-1}s^{-2}$. TKE and the Reynolds stresses both rely on a decomposition of the flow field into a average and fluctuating part, but the Reynolds stress computation is the ensemble average of different components of the fluctuating velocity field: $\sigma_{\text{Reynolds}} = \rho\tilde{u}_i\tilde{u}_j$. When turbulence is greatest, it is reasonable to assume the components of the fluctuating velocity fields are similar in magnitude ($|\tilde{u}_x| \approx |\tilde{u}_y| \approx |\tilde{u}_z|$). We can then relate TKE to σ_{Reynolds} as:

$$TKE = \frac{1}{2}\rho\left(\tilde{u}_x^2 + \tilde{u}_y^2 + \tilde{u}_z^2\right) \approx \frac{3}{2}\left(\rho\tilde{u}_i^2\right) = \frac{3}{2}\left(\sigma_{\text{Reynolds}}\right) \quad (25)$$

Thus, for TKE values greater than 6000 g/cms^2, we could expect hemolysis:

$$TKE_{threshold\ for\ hemolysis} = \frac{3}{2}\left(\sigma_{\text{Reynolds-threshold}}\right) = \frac{3}{2}\left(4000\frac{g}{cms^2}\right) = 6000\frac{g}{cms^2} \quad (26)$$

Patients 6 and 8 had the highest levels of TKE, which occurs during deceleration. The absolute maximum TKE value during deceleration for patients 6 and 8 under exercise conditions was 4761 g $cm^{-1}s^{-2}$ for patient 6 and 4234 g $cm^{-1}s^{-2}$ for patient 8. Therefore, it is expected that all Reynolds stresses are below the threshold for hemolysis. The TKE values during mid-deceleration under exercise conditions (when TKE is greatest) fall below this threshold.

Mesh and Temporal Independence Study

Our temporal independence study showed that MWSS and OSI varied little when quantified over cardiac cycles four through eight versus nine through thirteen; thus we think that quantifying results over five cardiac cycles is sufficient. The instantaneous velocities shown in Figure 12 demonstrate mesh independence of instantaneous velocity magnitude is unlikely in regions of non-zero TKE: The velocity field changed little at the suprarenal location, where TKE was virtually zero, but changed more dramatically at the mid-aneurysm location, where TKE was moderate. The MWSS and OSI appeared to nearly reach mesh independence at the SC location. It is important to note that the SC region was relatively “healthy” and experienced no turbulence in patient 1 (or in any of the other patients). Thus, it may be for that “normal” vasculature lacking complex or turbulent flow, quantifying

results over five cardiac cycles on an approximately 8.3-million element mesh is sufficient. Next, we observed that the MWSS decreased as the number of elements in the mesh increased at the IR, Mid-An and SB levels. This trend is opposite to that found in Tang et al.,[53] and may demonstrate that finer meshes resolve areas of flow stagnation near the wall in the aneurysmal and near-aneurysmal region. In these regions, it appears that the MWSS was approaching mesh independence, as the difference in MWSS between the 2.2 and 8.8-million element mesh and between the 8.3 and 31.8-million element mesh decreased. OSI, which is particularly sensitive to turbulence because it quantifies the unidirectionality of shear stress, did not reach or approach mesh independence at the IR, Mid-An, or SB location. It is possible that even finer meshes are needed for mesh independence of OSI. It is also likely that mesh independence is model-dependent, and that different mesh resolution are needed for different types of AAAs. Additional mesh independence studies are called for in future work. Nonetheless, it is clear that quantification of hemodynamics in AAAs over a single cardiac cycle on relatively coarse meshes grossly under describe–or even misrepresent–the hemodynamics in AAAs.

Comparison of Measured and Simulated Infrarenal Waveforms

Many computational studies of blood flow in AAAs utilize models of AAAs that begin at the IR level and end either at the SB level or a few centimeters distally in the common iliac arteries. Collecting patient-specific PCMRI data for both the SC and IR levels enables us to incorporate the upper branch vessels, which results in a more realistic, non-axisymmetric infrarenal flow pattern. Specifically, the celiac and SMA pull flow anteriorly, and the renal arteries draw flow laterally, and because the renal arteries exhibit constant antegrade flow, they draw flow from the infrarenal arteries, thus contributing to the retrograde flow in the infrarenal aorta at the beginning of diastole. While we will continue to improve the matching between simulated and measured IR flow, we think our method is more accurate than prescribing measured IR flow using an axisymmetric, nonphysiologic velocity profile, and represents an important step towards ensuring that the IR flow entering an AAA is as realistic as possible.

Limitations

Limitations to this analysis include the assumption of rigid wall, a Newtonian fluid, and a Womersley velocity profile at the inlet. In addition, during post-processing, we assume that any deviatoric velocity stems from turbulence, rather than numerical factors. We think that the use of a rigid wall in our analysis is an appropriate assumption, as many of our patients demonstrate significant thrombus and plaque in the aneurysm sac, which presumably limits motion: Long et al. found that the deformation at maximum AAA diameter to be on the order of 1.3 mm, which represents a 2.5% change in diameter over the cardiac cycle.[32] Nonetheless, we expect future incorporation of deformable walls to decrease wall shear stress, as found in a carotid artery study by Perktold et al.[44] Furthermore, we expect that the inclusion of a non-Newtonian fluid model to affect the shear stress, but minimally affect the pressures: Perktold and colleagues showed wall shear stress differences on the order of 10% for Newtonian versus non-Newtonian blood flow for the carotid artery,[43] while Khanafer et al found minimal differences in pressure (max=2.53%), but more significant differences in wall shear stress (max=26.7%) between non-Newtonian and Newtonian models of blood

flow in AAAs under resting conditions.[27] While we used a Womersley velocity profile for the inlet of our models, previous studies in healthy abdominal aortas revealed little difference in downstream MWSS and OSI when the PC-MRI data was mapped directly to the inflow face.[53] Furthermore, the assumption that deviatoric velocity mainly derive from turbulence, rather than numerical effects is confirmed by the fact that the TKE in the aorta is virtually zero superior to the aneurysm in 7 out of 8 AAAs during both rest and exercise, despite high velocities in this regions. In addition, although we feel that timestep size will affect the outlet flow and pressure waveforms very little, a more in-depth study of the how time-step size affects such quantities as point-wise velocity or wall shear stress is called for in future studies. Lastly, The mean pressure needed to define the R_p, C, and R_d values at each outlet is not known. This limitation results in the need to define these parameters via an iterative process, where the iterations are driven by target flows to each branch and SBP and DBP values at the inlet.

Despite these limitations, our work suggests that low, oscillatory shear is present at rest in the AAAs. These flow conditions are associated with atherosclerosis in the non-aneurysmal abdominal aorta, and are hypothesized to affect the progression of cerebral aneurysms.[7] Mild turbulence was also seen under resting conditions, agreeing with previous experimental results.[42] Exercise effectively eliminated the areas of low MWSS seen during rest. OSI decreased in the aneurysmal abdominal aorta between rest and exercise, but the OSI values we observed during exercise were higher than in the those observed in the young and old healthy abdominal aorta,[10,53] suggesting that perhaps complex recirculation zones exist throughout the aneurysmal abdominal aorta. We postulate that the moderate turbulence during exercise may reduce areas of flow stagnation, and that the mild increase in pressure associated with turbulent flow is not a concern for exercising patients. In addition, it appears that for most patients, the AAA itself introduced the turbulence, as the TKE in the aorta was virtually zero proximal to the AAA for 7 out of 8 patients for both rest and exercise.

Future Work: Computational Modeling

Future work calls for a direct 3-D segmentation and model construction method, incorporation of deformable wall simulations that match measured aortic luminal motion and measured wall thickness, and incorporation of a non-Newtonian model of blood. In addition, our mesh independence study demonstrates the need for meshes greater than 8-million elements. In addition, a more in-depth analysis of the complex flow features within AAAs is needed. Also, an automatic method to tune for an exact match in infrarenal flow waveform would be useful, to ensure more accurate simulations.

Future Work: Elucidating AAA Growth Mechanisms

All of the patients enrolled in the NIH study will have follow up MR exams after three years. The NIH study design enables many intra- and inter-patient analyses. On an intra-patient basis, we hope to learn whether regions of low shear in a specific patient will correlate with areas of increased aneurysm growth over time, as has been found in intracranial aneurysms,[7] and whether regions of stagnant flow at baseline conditions correlate with areas of increased thrombus burden at later imaging sessions.[48] On an inter-patient basis, we hope to learn whether usual-activity patients with lower-than-average shear and higher-than-average OSI

have increased AAA growth compared to their higher-than-average shear and lower-than average OSI peers. Additionally, because spinal cord injury patients have both reduced iliac artery caliber and a higher rate of AAA, it would be of interest to determine if small iliac size in ambulatory AAA patients correlates with increased growth. Lastly, because of the wide variety of AAA morphologies, we need to extend this analysis to additional patients so that differences in general AAA shape–fusiform versus bi-lobed versus single lobed–may be elucidated.

Conclusion

In conclusion, the methods outlined in this paper describe a more accurate process of simulation that incorporate patient-specific geometries, volumetric flows, and pressures and utilize meshes more than an order of magnitude larger than previous studies. The use of MRI data provided a non-invasive means to model blood flow in a highly patient specific manner, whereas the use of computational simulation enabled the study of blood flow at resolution many times finer than any imaging modality. We presented results from simulations of blood flow in eight patients during rest and exercise, and averaged results over five cardiac cycles, thus providing a more global picture of AAA hemodynamics than studies with only a few patients with results presented for a single cardiac cycle. The morphology of the AAAs varied widely from patient to patient, and none of the aneurysms in this study resembled the “textbook” shape frequently seen in studies of idealized AAAs. Furthermore, the inclusion of both SC and IR flow waveforms enabled inclusion of the upper branch vessels, which, in turn, lead to more realistic, nonaxisymmetric IR flow. This study demonstrates that exercise *may* positively alter the hemodynamic conditions hypothesized to induce aneurysm growth: The low, oscillatory, flow seen at rest, which is hypothesized to be associated with aneurysm growth, was largely eliminated during exercise. Furthermore, it is possible that the moderate turbulence seen during exercise may reduce thrombus deposition and growth. Because the larger scope of this study requires repeat imaging sessions at 3 years, this investigation will serve as a hemodynamic baseline for a variety of inter- and intra patient analysis that may help further elucidate the mechanisms behind abdominal aortic aneurysm growth.

Acknowledgments

The authors would like to thank Victoria Yeh and Allen Chiou for their assistance in constructing the computer models, and Sandra Rodriguez, Romi Samra, Anne Sawyer, Dr. Janice Yeung, Dr. Geoffrey Schultz, and Dr. Byard Edwards and all staff at the Lucas Center at Stanford University for assistance with imaging. This work was supported by the National Institutes of Health (Grants P50 HL083800, 2RO1 HL064338, P41 RR09784, and U54 GM072970) and the National Science Foundation (0205741, and CNS-0619926 for computer resources).

Abbreviations

AAA	Abdominal aortic aneurysm
DBP	Diastolic blood pressure
IR	Infrarenal
Mid-An	Mid-Aneurysm
MRI	Magnetic resonance imaging

MWSS	Mean wall shear stress
OSI	Oscillatory shear index
SB	Suprabifurcation
SBP	Systolic blood pressure
SC	Supraceliac
TKE	Turbulent kinetic energy

References

1. Allardice JT, Allwright GJ, Wafula JM, Wyatt AP. High prevalence of abdominal aortic aneurysm in men with peripheral vascular disease: Screening by ultrasonography. Brit. J. Surg. 1988; 75:240–2. [PubMed: 3280095]
2. Asbury CL, Ruberti JW, Bluth EI, Peattie RA. Experimental investigation of steady flow in rigid models of abdominal aortic aneurysms. Ann Biomed Eng. 1995; 23:29–39. [PubMed: 7762880]
3. Bax L, Bakker CJ, Klein WM, Blanken N, Beutler JJ, Mali WP. Renal blood flow measurements with use of phase-contrast magnetic resonance imaging: Normal values and reproducibility. J. Vasc. Interv. Radiol. 2005; 16:807–14. [PubMed: 15947044]
4. Berguer R, Bull JL, Khanafer K. Refinements in mathematical models to predict aneurysm growth and rupture. Ann. N.Y. Acad. Sci. 2006; 1085:110–6. [PubMed: 17182927]
5. Bluestein D, Niu L, Schoephoerster RT, Dewanjee MK. Steady flow in an aneurysm model: Correlation between fluid dynamics and blood platelet deposition. Journal of Biomechamical Engineering. 1996; 118:280–6.
6. Bluth EI, Murphey SM, Hollier LH, Sullivan MA. Color flow doppler in the evaluation of aortic aneurysms. Int. Angiol. 1990; 9:8–10. [PubMed: 2212801]
7. Boussel L, Rayz V, McCulloch C, Martin A, Acevedo-Bolton G, Lawton M, Higashida R, Smith WS, Young WL, Saloner D. Aneurysm growth occurs at region of low wall shear stress: Patient-specific correlation of hemodynamics and growth in a longitudinal study. Stroke. 2008; 39:2997–3002. [PubMed: 18688012]
8. Brady AR, Thompson SG, Fowkes FG, Greenhalgh RM, Powell JT. Abdominal aortic aneurysm expansion: Risk factors and time intervals for surveillance. Circulation. 2004; 110:16–21. [PubMed: 15210603]
9. Brewster DC, Cronenwett JL, Hallett JW Jr. Johnston KW, Krupski WC, Matsumura JS. Guidelines for the treatment of abdominal aortic aneurysms. Report of a subcommittee of the joint council of the american association for vascular surgery and society for vascular surgery. J. Vasc. Surg. 2003; 37:1106–17. [PubMed: 12756363]
10. Cheng CP, Herfkens RJ, Taylor CA. Abdominal aortic hemodynamic conditions in healthy subjects aged 50-70 at rest and during lower limb exercise: In vivo quantification using mri. Atherosclerosis. 2003; 168:323–31. [PubMed: 12801616]
11. Cornhill JF, Herderick EE, Stary HC. Topography of human aortic sudanophilic lesions. Monogr. Atheroscler. 1990; 15:13–9. [PubMed: 2296239]
12. Curci JA, Thompson RW. Adaptive cellular immunity in aortic aneurysms: Cause, consequence, or context? J. Clin. Invest. 2004; 114:168–171. [PubMed: 15254583]
13. Dalman RL, Tedesco MM, Myers J, Taylor CA. Aaa disease: Mechanism, stratification, and treatment. Ann. N.Y. Acad. Sci. 2006; 1085:92–109. [PubMed: 17182926]
14. Draney MT, Alley MT, Tang BT, Wilson NM, Herfkens RJ, Taylor CA. International Society for Magnetic Resonance in Medicine. Honolulu, HI: 2002. Importance of 3d nonlinear gradient corrections for quantitative analysis of 3d mr angiographic data.

15. Egelhoff CJ, Budwig RS, Elger DF, Khraishi TA, Johansen KH. Model studies of the flow in abdominal aortic aneurysms during resting and exercise conditions. J. Biomech. 1999; 32:1319–29. [PubMed: 10569710]
16. Finol EA, Keyhani K, Amon CH. The effect of asymmetry in abdominal aortic aneurysms under physiologically realistic pulsatile flow conditions. J. Biomech. Eng. 2003; 125:207–17. [PubMed: 12751282]
17. Fleming C, Whitlock EP, Beil TL, Lederle FA. Screening for abdominal aortic aneurysm: A best-evidence systematic review for the us preventive services task force. Ann. Intern. Med. 2005; 142:203–11. [PubMed: 15684209]
18. Gillum RF. Epidemiology of aortic aneurysm in the united states. J. Clin. Epidemiol. 1995; 48:1289–98. [PubMed: 7490591]
19. Hance KA, Tataria M, Ziporin SJ, Lee JK, Thompson RW. Monocyte chemotactic activity in human abdominal aortic aneurysms: Role of elastin degradation peptides and the 67-kd cell surface elastin receptor. J. Vasc. Surg. 2002; 35:254–61. [PubMed: 11854722]
20. He X, Ku DN. Pulsatile flow in the human left coronary artery bifurcation: Average conditions. J. Biomech. Eng. 1996; 118:74–82. [PubMed: 8833077]
21. Holenstein R, Ku DN. Reverse flow in the major infrarenal vessels - a capacitive phenomenon. Biorheology. 1988; 25:835–842. [PubMed: 3076804]
22. Hope SA, Tay DB, Meredith IT, Cameron JD. Waveform dispersion, not reflection, may be the major determinant of aortic pressure wave morphology. Am. J. Physiol. Heart. Circul. Physiol. 2005; 289:H2497–502.
23. Hoshina K, Sho E, Sho M, Nakahashi TK, Dalman RL. Wall shear stress and strain modulate experimental aneurysm cellularity. J. Vasc. Surg. 2003; 37:1067–74. [PubMed: 12756356]
24. Hughes TJ. The finite element method: Linear static and dynamic finite element analysis. Dover Publications; Mineola, NY: 2000. 107
25. Humphrey JD, Taylor CA. Intracranial and abdominal aortic aneurysms: Similarities, differences, and need for a new class of computational models. Annu. Rev. Biomed. Eng. 2008; 10:221–46. [PubMed: 18647115]
26. Khanafer KM, Bull JL, Upchurch GR Jr. Berguer R. Turbulence significantly increases pressure and fluid shear stress in an aortic aneurysm model under resting and exercise flow conditions. Ann. Vasc. Surg. 2007; 21:67–74. [PubMed: 17349339]
27. Khanafer KM, Gadhoke P, Berguer R, Bull JL. Modeling pulsatile flow in aortic aneurysms: Effect of non-newtonian properties of blood. Biorheology. 2006; 43:661–79. [PubMed: 17047283]
28. Kim HJ, Figueroa CA, Hughes TJR, Jansen KE, Taylor CA. Augmented lagrangian method for constraining the shape of velocity profiles at outlet boundaries for three-dimensional finite element simulations of blood flow. Comput. Meth. Appl. Mech. Eng. 2009; 198:3551–3566.
29. Koch AE, Kunkel SL, Pearce WH, Shah MR, Parikh D, Evanoff HL, Haines GK, Burdick MD, Strieter RM. Enhanced production of the chemotactic cytokines interleukin-8 and monocyte chemoattractant protein-1 in human abdominal aortic aneurysms. Am. J. Pathol. 1993; 142:1423–31. [PubMed: 8494046]
30. Laskey WK, Parker HG, Ferrari VA, Kussmaul WG, Noordergraaf A. Estimation of total systemic arterial compliance in humans. J. Appl. Physiol. 1990; 69:112–9. [PubMed: 2394640]
31. Lederle FA, Johnson GR, Wilson SE, Chute EP, Hye RJ, Makaroun MS, Barone GW, Bandyk D, Moneta GL, Makhoul RG. The aneurysm detection and management study screening program: Validation cohort and final results. Aneurysm detection and management veterans affairs cooperative study investigators. Arch. Intern. Med. 2000; 160:1425–30. [PubMed: 10826454]
32. Long A, Rouet L, Vitry F, Albertini JN, Marcus C, Clement C. Compliance of abdominal aortic aneurysms before and after stenting with tissue doppler imaging: Evolution during follow-up and correlation with aneurysm diameter. Ann. Vasc. Surg. 2009; 23:49–59. [PubMed: 18973982]
33. Miller FJ Jr. Sharp WJ, Fang X, Oberley LW, Oberley TD, Weintraub NL. Oxidative stress in human abdominal aortic aneurysms: A potential mediator of aneurysmal remodeling. Arterioscler. Thromb. Vasc. Biol. 2002; 22:560–5. [PubMed: 11950691]
34. Montain SJ, Jilka SM, Ehsani AA, Hagberg JM. Altered hemodynamics during exercise in older essential hypertensive subjects. Hypertension. 1988; 12:479–84. [PubMed: 3192293]

35. Moore JE Jr. Ku DN. Pulsatile velocity measurements in a model of the human abdominal aorta under resting conditions. J. Biomech. Eng. 1994; 116:337–46. [PubMed: 7799637]
36. Moore JE Jr. Xu C, Glagov S, Zarins CK, Ku DN. Fluid wall shear stress measurements in a model of the human abdominal aorta: Oscillatory behavior and relationship to atherosclerosis. Atherosclerosis. 1994; 110:225–40. [PubMed: 7848371]
37. Muller J, Sahni O, Li X, Jansen KE, Shephard MS, Taylor CA. Anisotropic adaptive finite element method for modelling blood flow. Comput. Meth. Biomech. Biomed. Eng. 2005; 8:295–305.
38. Myers J, Prakash M, Froelicher V, Do D, Partington S, Atwood JE. Exercise capacity and mortality among men referred for exercise testing. New. Engl. J. Med. 2002; 346:793–801. [PubMed: 11893790]
39. Nakahashi TK, Hoshina K, Tsao PS, Sho E, Sho M, Karwowski JK, Yeh C, Yang RB, Topper JN, Dalman RL. Flow loading induces macrophage antioxidative gene expression in experimental aneurysms. Arterioscler. Thromb. Vasc. Biol. 2002; 22:2017–22. [PubMed: 12482828]
40. Newman KM, Jean-Claude J, Li H, Ramey WG, Tilson MD. Cytokines that activate proteolysis are increased in abdominal aortic aneurysms. Circulation. 1994; 90:II224–7. [PubMed: 7955258]
41. Nichols WW, O'Rourke MF. Mcdonald's blood flow in arteries. 4th ed.. Oxford University Press; New York: 1998. 179
42. Peattie RA, Riehle TJ, Bluth EI. Pulsatile flow in fusiform models of abdominal aortic aneurysms: Flow fields, velocity patterns and flow-induced wall stresses. J. Biomech. Eng. 2004; 126:438–46. [PubMed: 15543861]
43. Perktold K, Peter RO, Resch M, Langs G. Pulsatile non-newtonian blood flow in three-dimensional carotid bifurcation models: A numerical study of flow phenomena under different bifurcation angles. J. Biomed. Eng. 1991; 13:507–15. [PubMed: 1770813]
44. Perktold K, Rappitsch G. Computer simulation of local blood flow and vessel mechanics in a compliant carotid artery bifurcation model. J. Biomech. 1995; 28:845–56. [PubMed: 7657682]
45. Rayz VL, Boussel L, Lawton MT, Acevedo-Bolton G, Ge L, Young WL, Higashida RT, Saloner D. Numerical modeling of the flow in intracranial aneurysms: Prediction of regions prone to thrombus formation. Ann. Biomed. Eng. 2008; 36:1793–804. [PubMed: 18787954]
46. Sallam AM, Hwang NHC. Human red blood-cell hemolysis in a turbulent shear- flow - contribution of reynolds shear stresses. Biorheology. 1984; 21:783–797. [PubMed: 6240286]
47. Salsac AV, Sparks SR, Chomaz JM, Lasheras JC. Evolution of the wall shear stresses during the progressive enlargement of symmetric abdominal aortic aneurysms. J. Fluid. Mech. 2006; 560:19–51.
48. Salsac AV, Sparks SR, Lasheras JC. Hemodynamic changes occurring during the progressive enlargement of abdominal aortic aneurysms. Ann. Vasc. Surg. 2004; 18:14–21. [PubMed: 14712379]
49. Santilli JD, Santilli SM. Diagnosis and treatment of abdominal aortic aneurysms. Am. Fam. Physician. 1997; 56:1081–90. [PubMed: 9310060]
50. Sergeev SI. Fluid oscillations in pipes at moderate reynolds numbers. Fluid Dyn. 1966; 1:21–22.
51. Steele BN, Olufsen MS, Taylor CA. Fractal network model for simulating abdominal and lower extremity blood flow during resting and exercise conditions. Comput. Meth. Biomech. Biomed. Eng. 2007; 10:39–51.
52. Stergiopulos N, Segers P, Westerhof N. Use of pulse pressure method for estimating total arterial compliance in vivo. Am. J. Physiol. Heart. Circul. Physiol. 1999; 276:H424–H428.
53. Tang BT, Cheng CP, Draney MT, Wilson NM, Tsao PS, Herfkens RJ, Taylor CA. Abdominal aortic hemodynamics in young healthy adults at rest and during lower limb exercise: Quantification using image-based computer modeling. Am. J. Physiol. Heart. Circul. Physiol. 2006; 291:H668–76.
54. Taylor CA, Cheng CP, Espinosa LA, Tang BT, Parker D, Herfkens RJ. In vivo quantification of blood flow and wall shear stress in the human abdominal aorta during lower limb exercise. Ann. Biomed. Eng. 2002; 30:402–8. [PubMed: 12051624]
55. Taylor CA, Draney MT. Experimental and computational methods in cardiovascular fluid mechanics. Annu. Rev. Fluid. Mech. 2004; 36:197–231.

56. Taylor CA, Hughes TJR, Zarins CK. Finite element modeling of three- dimensional pulsatile flow in the abdominal aorta: Relevance to atherosclerosis. Ann. Biomed. Eng. 1998; 26:975–87. [PubMed: 9846936]
57. Taylor CA, Steinman DA. Image-based modeling of blood flow and vessel wall dynamics: Applications, methods and future directions. Ann. Biomed. Eng. 2009 In Press.
58. Taylor TW, Yamaguchi T. Three-dimensional simulation of blood flow in an abdominal aortic aneurysm--steady and unsteady flow cases. J. Biomech. Eng. 1994; 116:89–97. [PubMed: 8189719]
59. Thompson RW, Holmes DR, Mertens RA, Liao S, Botney MD, Mecham RP, Welgus HG, Parks WC. Production and localization of 92-kilodalton gelatinase in abdominal aortic aneurysms. An elastolytic metalloproteinase expressed by aneurysm infiltrating macrophages. J. Clin. Invest. 1995; 96:318–26. [PubMed: 7615801]
60. van der Molen AJ. Nephrogenic systemic fibrosis and the role of gadolinium contrast media. J. Med. Imaging. Radiot. Oncol. 2008; 52:339–50.
61. Vignon-Clementel IE, Figueroa CA, Jansen KC, T. C.A. Outflow boundary conditions for three-dimensional finite element modeling of blood flow and pressure in arteries. Comput. Meth. Appl. Mech. Eng. 2006; 195:3776–3796.
62. Vignon-Clementel IE, Figueroa CA, Jensen KE, Taylor CA. Outflow boundary conditions for three-dimensional simulations of non-periodic blood flow and pressure fields in deformable arteries. Comput. Meth. Biomech. Biomed. Eng. 2009 In Press.
63. Vollmar JF, Paes E, Pauschinger P, Henze E, Friesch A. Aortic aneurysms as late sequelae of above-knee amputation. Lancet. 1989; 2:834–5. [PubMed: 2571760]
64. Whiting CH, Jansen KC. A stabilized finite element method for the incompressible navier-stokes equations using a hierarchical basis. Int. J. Numer. Meth. Fluid. 2001; 35:93–116.
65. Wilson N, Wang K, Dutton RW, Taylor CA. A software framework for creating patient specific geometric models from medical imaging data for simulation based medical planning of vascular surgery. Lecture Notes In Computer Science. 2001; 2208:449–456.
66. Womersley JR. Method for the calculation of velocity, rate of flow and viscous drag in arteries when the pressure gradient is known. J. Physiol. 1955; 127:553–63. [PubMed: 14368548]
67. Yeung JJ, Kim HJ, Abbruzzese TA, Vignon-Clementel IE, Draney-Blomme MT, Yeung KK, Perkash I, Herfkens RJ, Taylor CA, Dalman RL. Aortoiliac hemodynamic and morphologic adaptation to chronic spinal cord injury. J. Vasc. Surg. 2006; 44:1254–1265. [PubMed: 17145427]

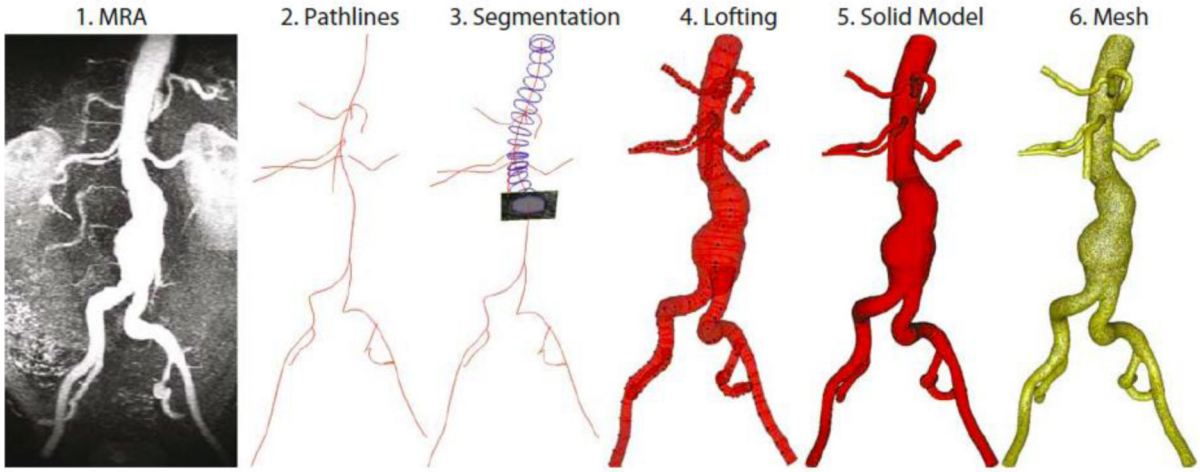

Figure 1.

Building a model from the MRA data (1) entails generating pathlines (2), segmenting along the pathlines (3), lofting the segmentations to create vessels (4), unioning the vessels to create a single, solid model representing the flow domain (5), and then discretizing the model into a finite-element mesh (6).

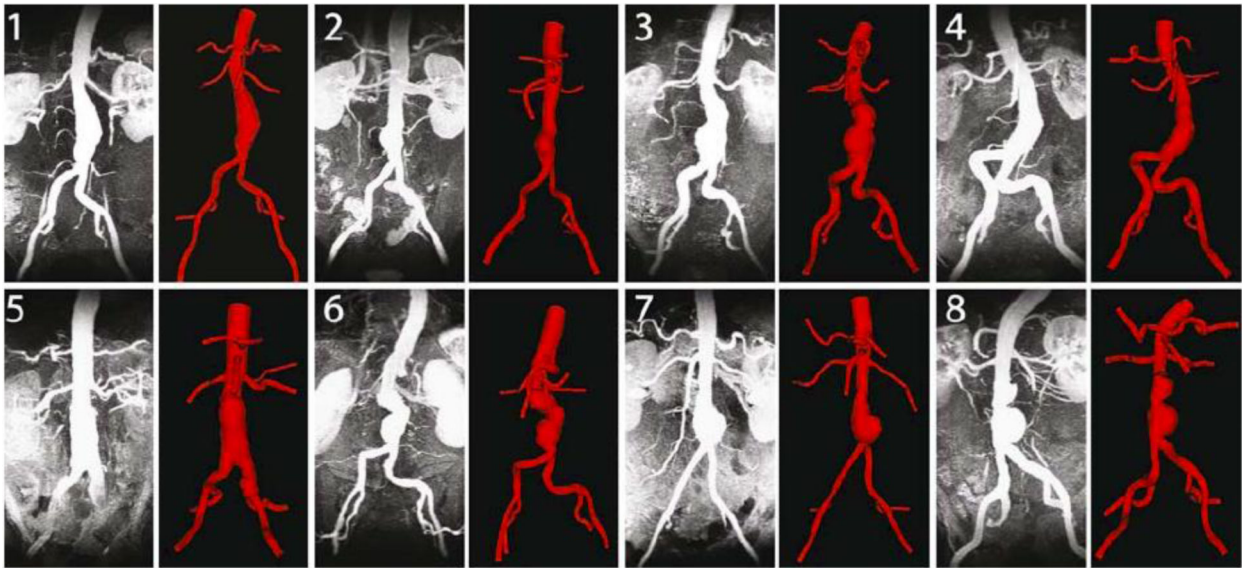

Figure 2.
The maximum intensity projection (MIP) of the MRA is compared to the 3-D computer model for all eight patients.

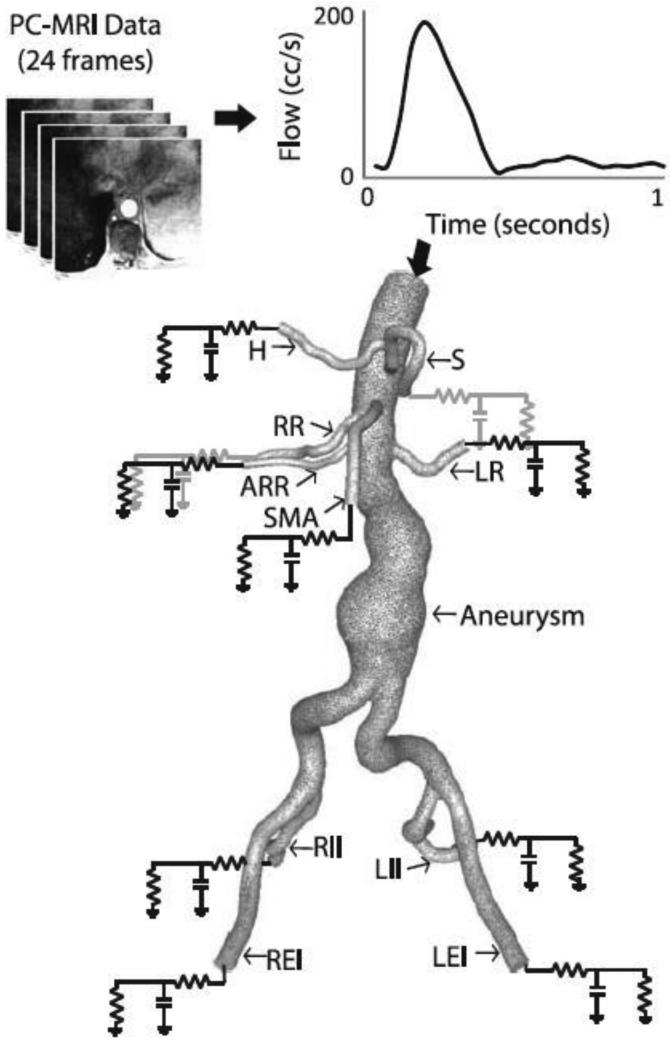

Figure 3.

A patient-specific SC flow waveform measured by phase-contrast MRI (resting conditions) is mapped to the inflow face using a Womersley velocity profile. A patient-specific 3-element Windkessel model with a proximal resistance (Rp), capacitance (C), distal resistance (Rd) boundary condition is used to represent the resistance and compliance of the vasculature downstream of each outlet. The outlet labels are as follows: S=splenic artery, LR=left renal artery, LEI=left external iliac artery, LII=left internal iliac artery, RII=right internal iliac artery, REI=right external iliac artery, SMA=superior mesenteric artery, ARR=accessory right renal artery (Note: accessory renals are not found in the majority of patients), RR=right renal artery, H=hepatic artery. Please note that typically (as in this patient), the splenic and hepatic arteries branch from a common celiac trunk.

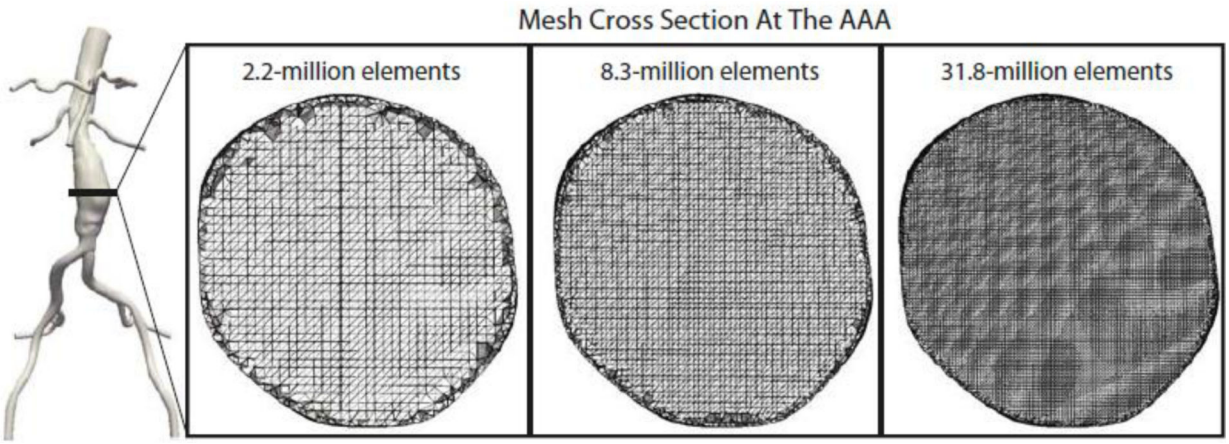

Figure 4.
Cross sections of the 2.2, 8.3, and 31.8-million finite-element meshes are shown at the mid-aneurysm level for patient 1.

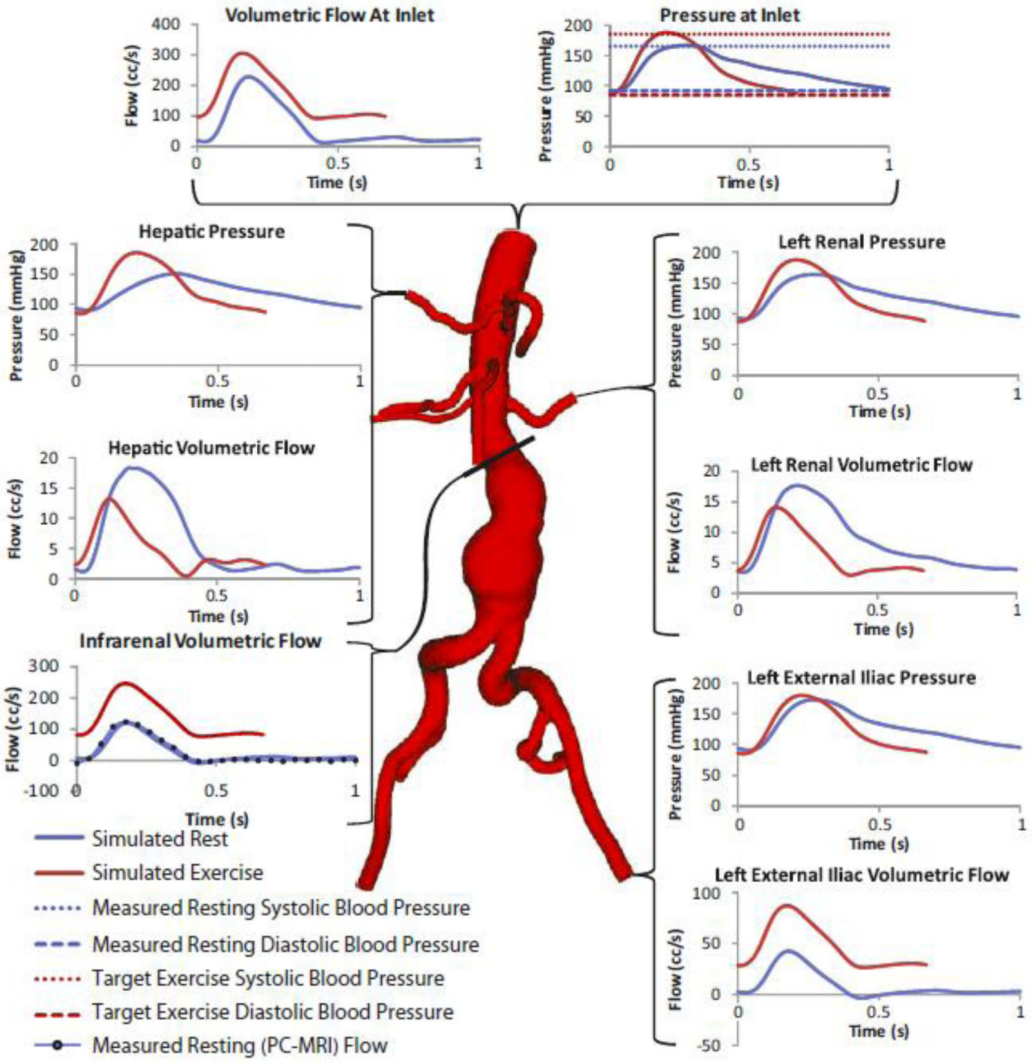

Figure 5.

Pressure and flow waveforms at the inlet and selected outlets of patient 3 under rest and exercise conditions. The pressure waveforms at each outlet were calculated by averaging the pressure field over the outlet area. The flow waveforms at each outlet were calculated by integrating the velocities over the outlet area. The flow and pressure waves depicted in this figure show a number of physiologically-realistic features. For instance, for the renal arteries under resting conditions and the abdominal aorta under exercise conditions, the flow waveforms lack backflow and have a relatively high diastolic flow, matching literature measurements and calculations.[3,21] In addition, not only are the outlet pressures in the physiologic range, the inlet resting maximum and minimum pressures agree well with the measured systolic and diastolic pressure, and the inlet exercise maximum and minimum pressure agree well with the physiologic target systolic and diastolic pressures.

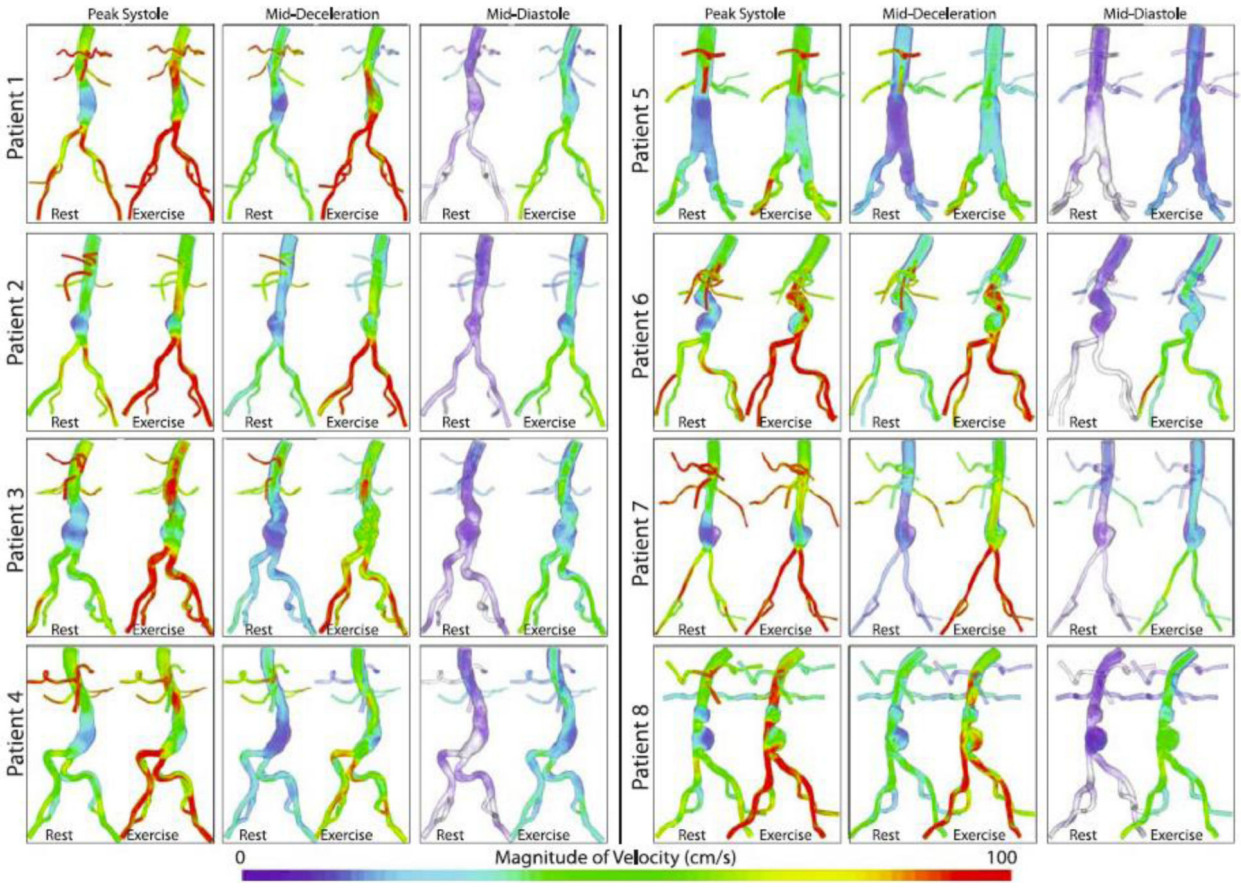

Figure 6.

The magnitude of the ensemble average of the velocity field at three points in the cardiac cycle (peak systole, mid-deceleration, and mid-diastole) is plotted using a volume rendering technique for all patients for both rest and exercise. In general, the flow features look more complex during exercise than during rest, for all three reported time points. In particular, during exercise, features such as jets and recirculation zones can be observed, especially during diastole and mid-deceleration.

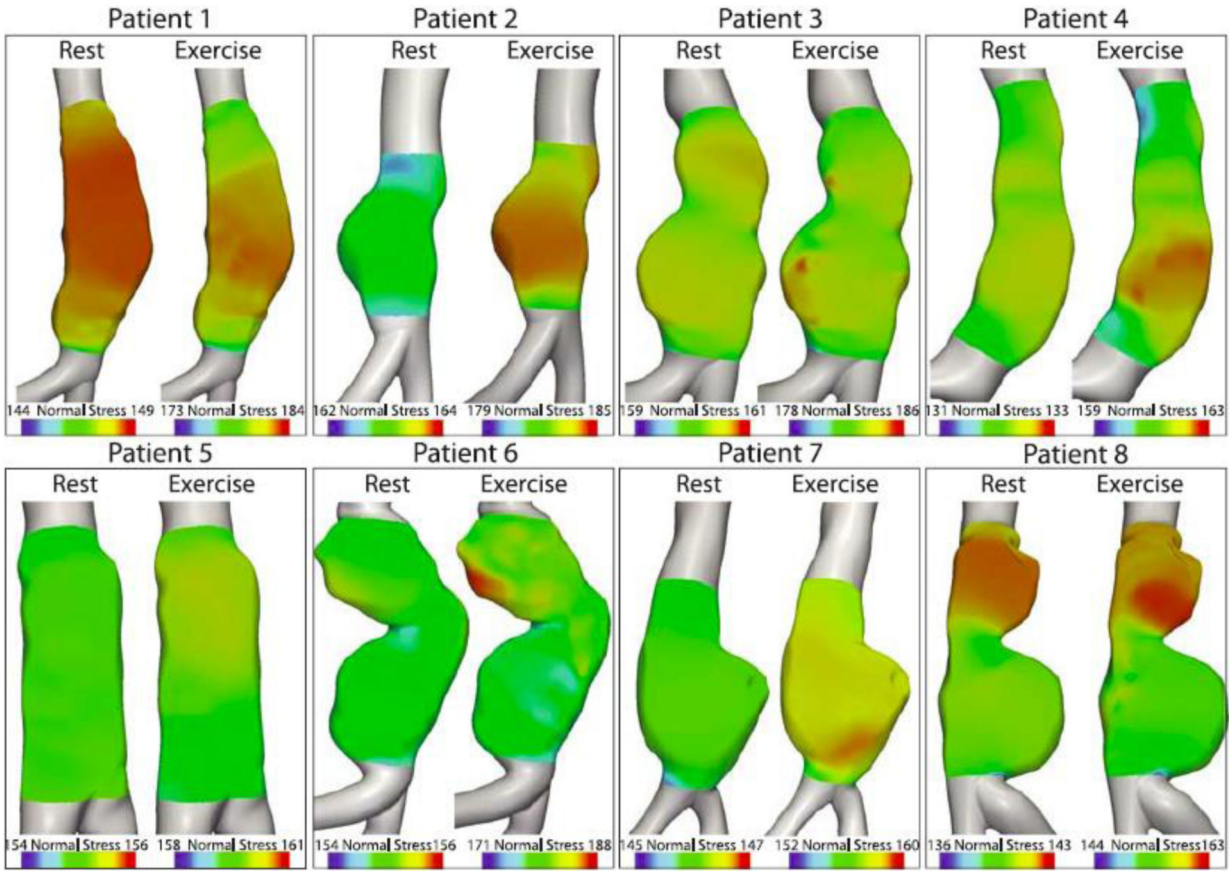

Figure 7.

The distribution of normal stresses acting on the luminal wall of the aneurysms at peak flow (defined as peak systole throughout the paper) is shown for both rest and exercise. Values are presented in mmHg.

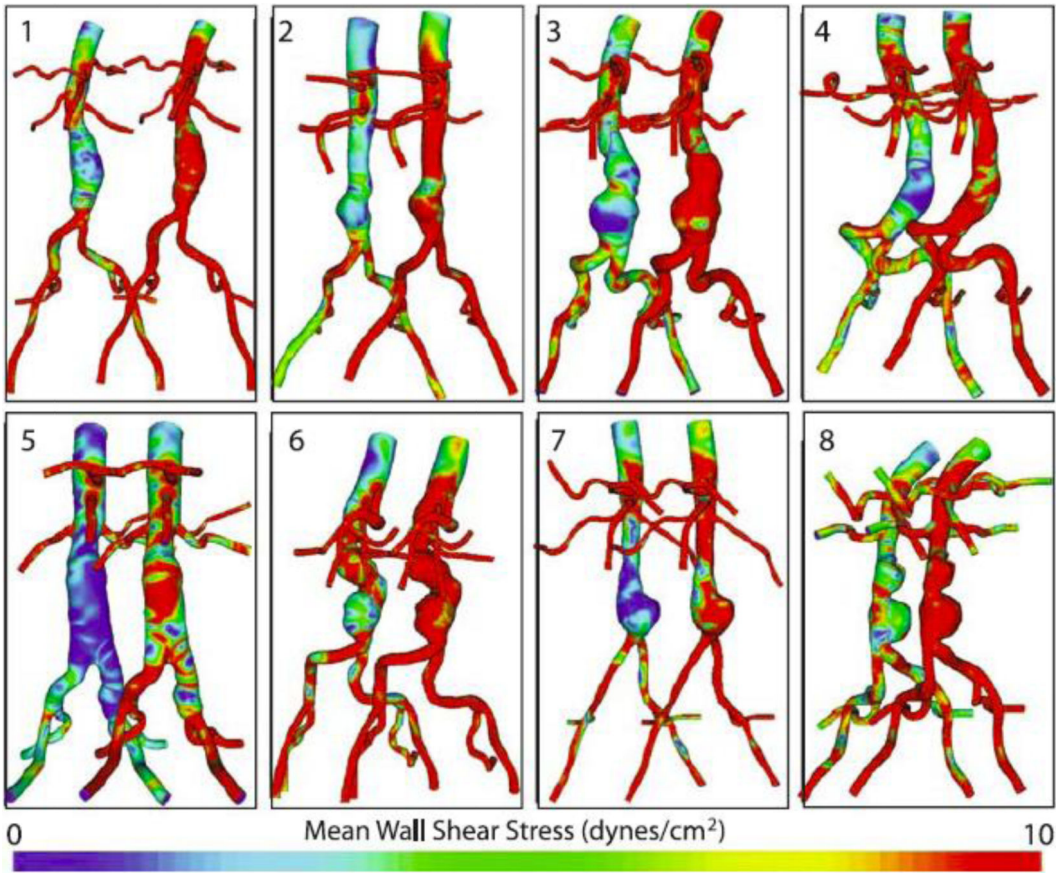

Figure 8.

Mean wall shear stress (MWSS) for rest (left of each pair) and exercise (right of each pair) is shown for all eight patients. MWSS was quantified from cardiac cycles four through eight.

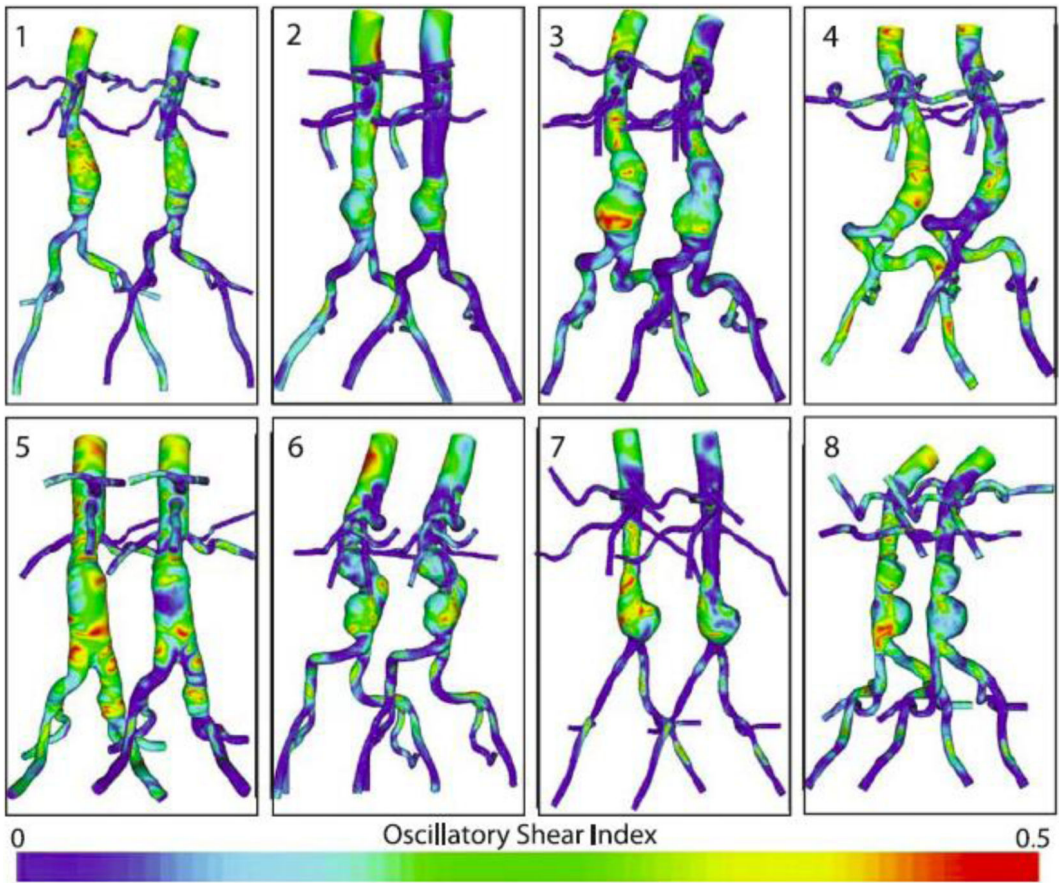

Figure 9.
Oscillatory shear index (OSI) for rest (left of each pair) and exercise (right of each pair) is shown for all eight patients. OSI was quantified from cardiac cycles four through eight.

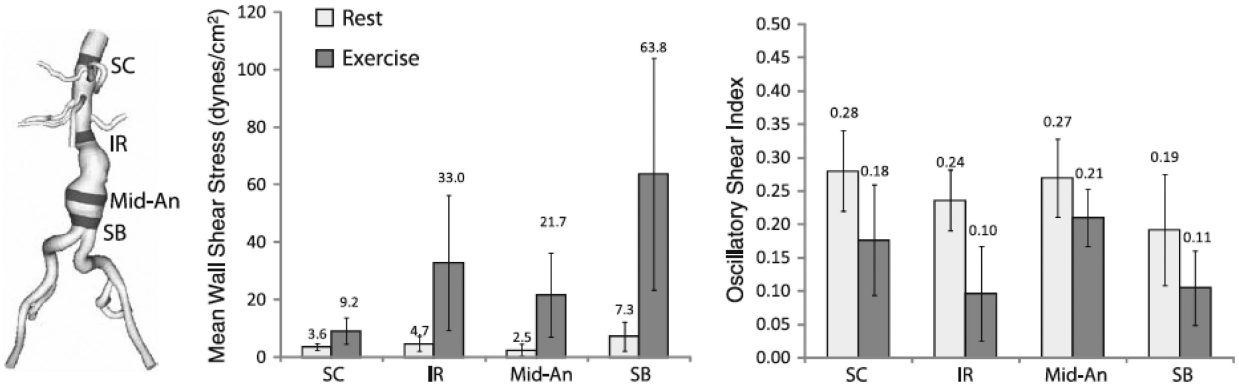

Figure 10.

Mean wall shear stress (left) and oscillatory shear index (right) values were quantified in 1-cm strips at four locations (SC=supraceliac, IR=infrarenal, Mid-An=mid-aneurysm, SB=suprabifurcation) for rest and exercise. The location of the strips for patient 3 are shown at left. The standard deviation for each value are indicated with vertical bars. MWSS and OSI were quantified from cardiac cycles four through eight.

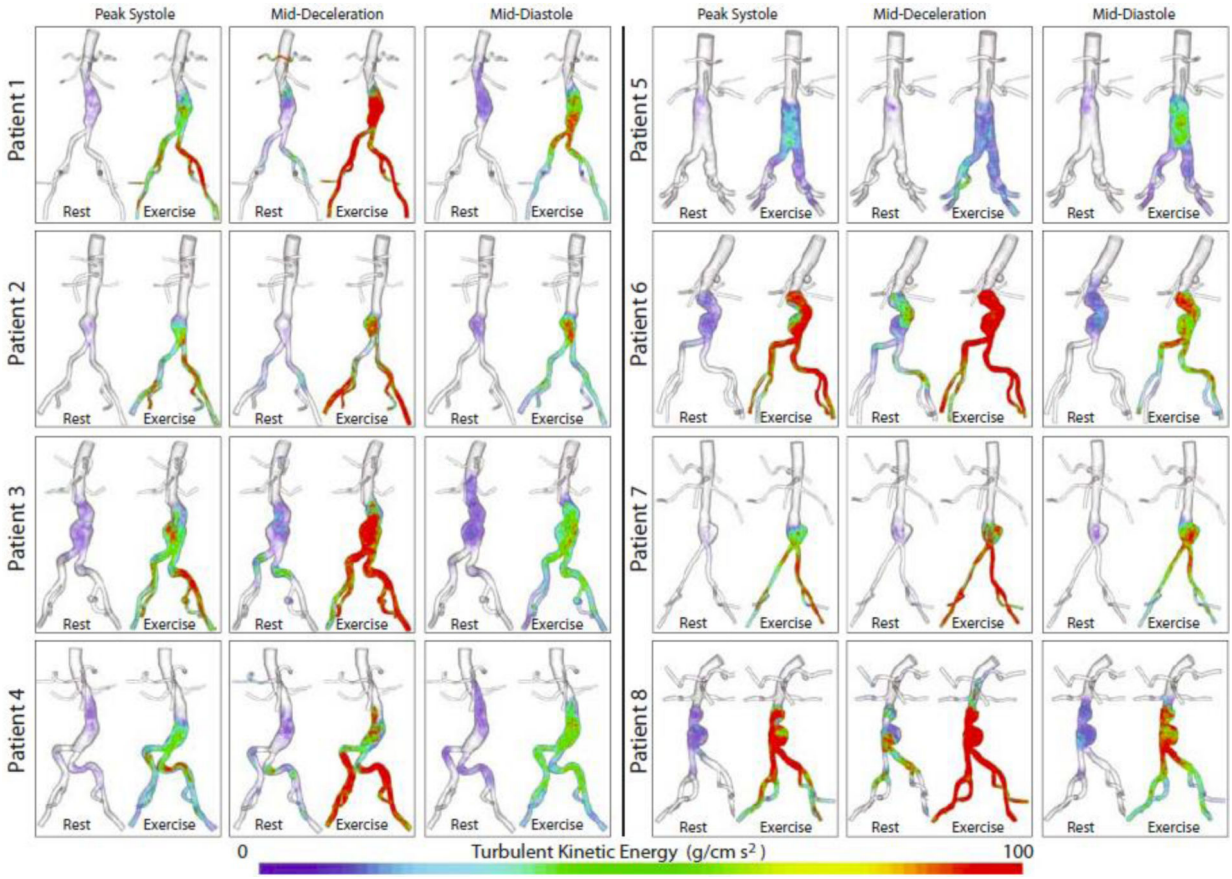

Figure 11.

Turbulent kinetic energy (TKE) at three points in the cardiac cycle (peak systole, mid-deceleration, and mid-diastole) are plotted for all patients for both rest and exercise. TKE was quantified from cardiac cycles four through eight.

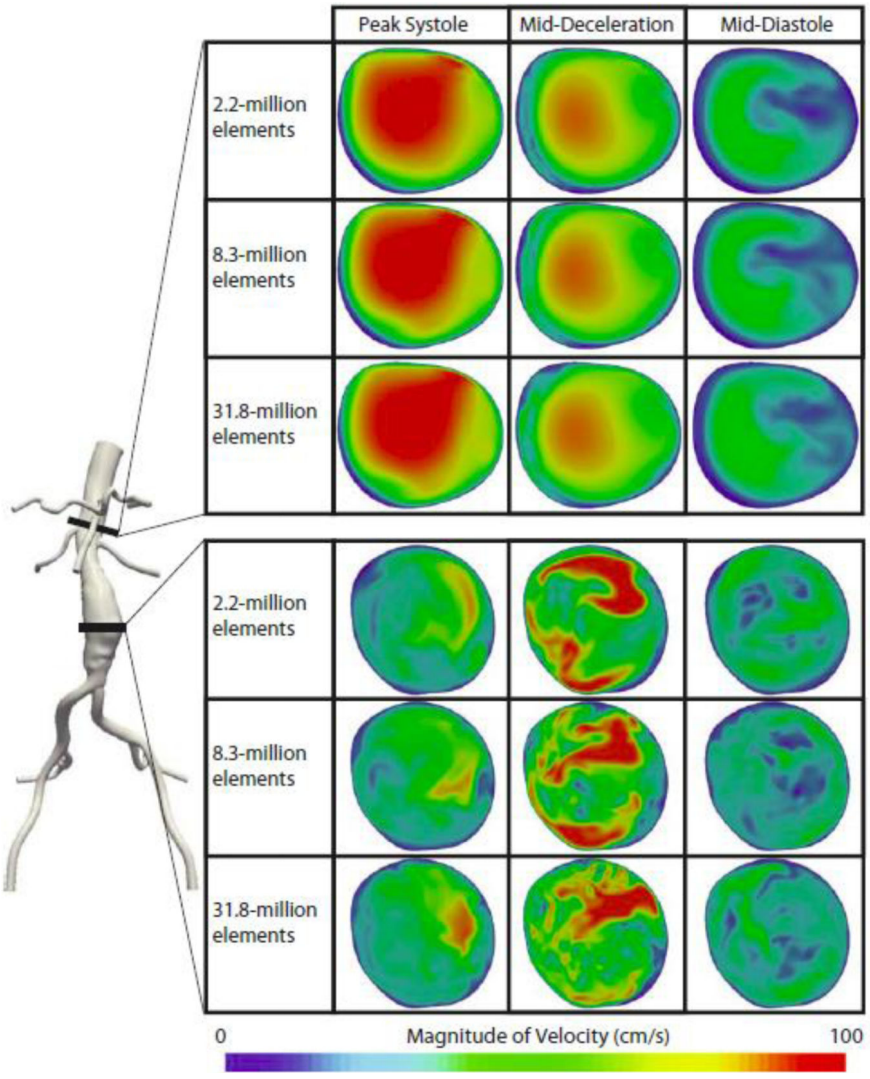

Figure 12.

The instantaneous magnitude of the velocity field for the eighth cardiac cycle of patient 1 under exercise conditions are shown at the mid-aneurysm and suprarenal locations for the 2.2, 8.3, and 31.8-million finite-element meshes at peak systole, mid-deceleration, and mid-diastole. The velocity field changed little between meshes at the suprarenal location, where the TKE was virtually zero, but changed more dramatically at the mid-aneurysm location where TKE was moderate. Mesh independence of the instantaneous velocity fields is not achievable in turbulent regions.

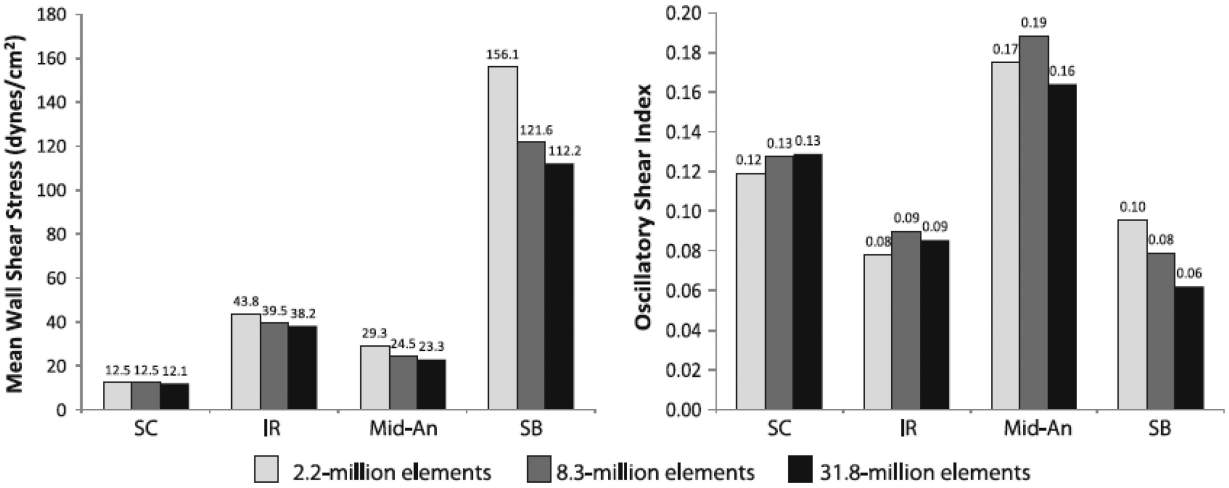

Figure 13.

Mean wall shear stress (left) and oscillatory shear index (right) at four locations (SC=supraceliac, IR=infrarenal, Mid-An=mid-aneurysm, SB=suprabifurcation) for three meshes (2.2-million, 8.3-million, and 31.8-million elements) are shown for patient 1 during exercise. MWSS and OSI were quantified from cardiac cycles four through eight.

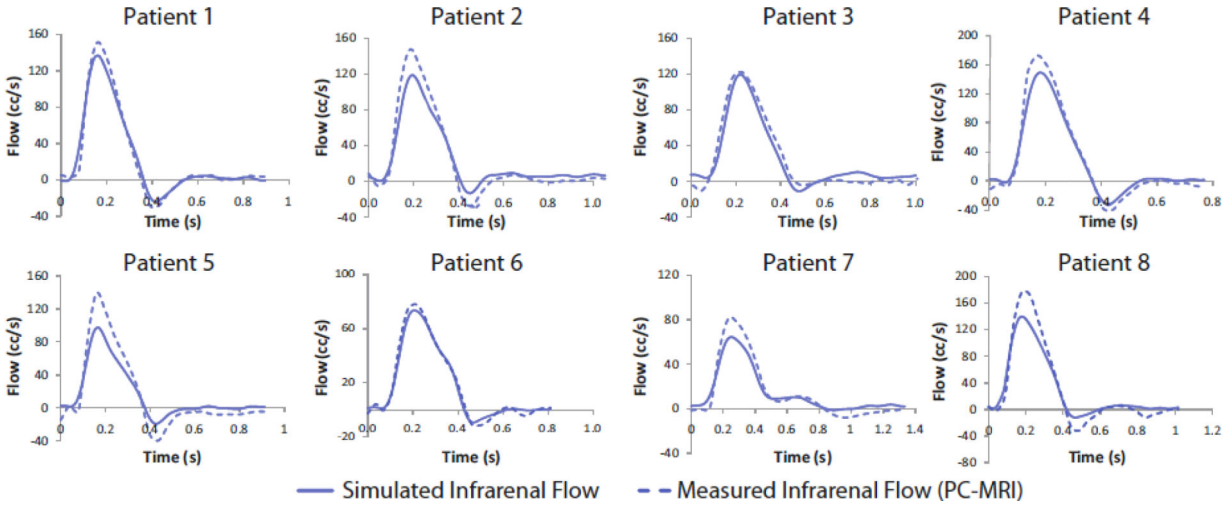

Figure 14.

A comparison between simulated and measured volumetric flow at the infrarenal level during rest for all eight patients is shown above.

Table 1

Reynolds and Womersley Numbers at the Supraceliac and Infrarenal Levels

Supraceliac	**mean**	**st. deviation**	**range**
Mean Reynolds Number	797.67	94.10	664.22 - 893.14
Systolic Reynolds Number	3035.73	485.25	2275.62 - 3647.57
Womersley Number	6.45	1.10	5.07 - 8.18

Infrarenal	**mean**	**st. deviation**	**range**
Mean Reynolds Number	316.19	68.72	222.18 - 404.60
Systolic Reynolds Number	1869.39	500.43	1118.24 - 2489.21
Womersley Number	5.87	1.40	3.25 - 7.55

Table 2

The spatial range of normal stresses at peak flow, the temporal range of the normal stresses over the cardiac cycle, and the ratio between the spatial and temporal ranges.

	Patient 1		Patient 2		Patient 3		Patient 4		Patient 5		Patient 6		Patient 7		Patient 8		Average	
	Rest	Exercise	Rest	Exercise	Rest	Exercise	Rest	Exercise	Rest	Exercise	Rest	Exercise	Rest	Exercise	Rest	Exercise	Rest	Exercise
Spatial Range of Normal Stresses On Aneurysm Lumen At peak Flow (mmHg)	2.92	8.95	1.29	5.19	1.20	5.73	0.75	3.48	0.46	1.11	1.94	14.0	1.57	6.38	6.67	18.3	2.10	7.89
Temporal Range of Normal Stresses On Aneurysm Lumen (mmHg)	69.4	100	71.0	97.3	77.8	102	53.3	84.9	71.3	94.5	78.1	101	57.7	82.2	44.7	72.7	65.4	92.0
% Spatial/Temporal Range	4.21	8.91	1.82	5.33	1.54	5.61	1.41	4.09	0.64	1.17	2.49	13.8	2.71	7.77	14.9	25.1	3.72	8.98

Table 3

Turbulent Kinetic Energy and Kinetic Energy Within The Abdominal Aorta and Aneurysm Of All Eight Patients At Three Points In the Cardiac Cycle For Both Rest And Exercise.

		Turbulent Kinetic Energy (g cm^{-1} s^{-2})					
		Rest			Exercise		
Patient #	AAA type	Systole	Mid-Decel.	Mid-Dias.	Systole	Mid-Decel.	Mid-Dias.
1	fusiform	1.75	4.96	3.31	24.61	255.42	51.23
2	single-lobed	0.73	0.60	1.56	8.68	27.13	20.68
3	bi-lobed	2.08	3.02	3.60	40.06	174.85	35.70
4	fusiform	1.47	1.66	2.00	21.15	43.10	39.78
5	fusiform	0.65	0.62	0.65	11.86	5.89	22.84
6	bi-lobed	3.79	17.33	6.07	183.84	410.78	72.08
7	single-lobed	0.51	0.82	0.90	16.39	46.76	41.23
8	bi-lobed	3.77	30.62	6.33	278.00	397.64	159.36
	mean	**1.84**	**7.45**	**3.05**	**73.07**	**170.19**	**55.36**
	st. deviation	**1.32**	**10.90**	**2.20**	**101.07**	**167.22**	**45.04**

		Kinetic Energy (g cm^{-1} s^{-2})					
		Rest			Exercise		
Patients	AAA type	Systole	Mid-Decel.	Mid-Dias.	Systole	Mid-Decel.	Mid-Dias.
1	fusiform	592.73	240.67	3.44	2333.56	2254.23	407.37
2	single-lobed	473.31	166.67	5.80	2004.16	1578.72	298.71
3	bi-lobed	314.90	104.45	6.34	1596.97	1321.53	313.56
4	fusiform	431.58	93.92	2.25	1713.19	1088.29	176.27
5	fusiform	125.93	28.01	1.88	404.11	366.98	53.54
6	bi-lobed	356.43	282.56	15.13	2381.10	1964.90	329.27
7	single-lobed	211.06	35.55	4.80	922.54	1244.05	183.91
8	bi-lobed	518.64	440.49	20.68	3123.75	2839.58	862.73
	Mean	**378.07**	**174.04**	**7.54**	**1809.92**	**1582.29**	**328.17**
	st. deviation	**157.52**	**140.93**	**6.75**	**860.46**	**763.65**	**242.73**

		TKE/KE Ratio					
		Rest			Exercise		
Patients	AAA type	Systole	Mid-Decel.	Mid-Dias.	Systole	Mid-Decel.	Mid-Dias.
1	fusiform	0.0029	0.0206	0.9644	0.0105	0.1133	0.1258
2	single-lobed	0.0015	0.0036	0.2688	0.0043	0.0172	0.0692
3	bi-lobed	0.0066	0.0289	0.5669	0.0251	0.1323	0.1139
4	fusiform	0.0034	0.0177	0.8895	0.0123	0.0396	0.2257
5	fusiform	0.0051	0.0221	0.3457	0.0293	0.0160	0.4266
6	bi-lobed	0.0106	0.0613	0.4014	0.0772	0.2091	0.2189
7	single-lobed	0.0024	0.0230	0.1881	0.0178	0.0376	0.2242

		TKE/KE Ratio					
		Rest			Exercise		
Patients	**AAA type**	**Systole**	**Mid-Decel.**	**Mid-Dias.**	**Systole**	**Mid-Decel.**	**Mid-Dias.**
8	bi-lobed	0.0073	0.0695	0.3063	0.0890	0.1400	0.1847
	Mean	**0.0050**	**0.0308**	**0.4914**	**0.0332**	**0.0881**	**0.1986**
	st. deviation	**0.0030**	**0.0226**	**0.2911**	**0.0320**	**0.0708**	**0.1090**